**INTERNATIONAL JOURNAL OF ADVANCED RESEARCH**
*International Peer-Reviewed Research Journal*
**ISSN (Online): 3106-7980 | ISSN (Print): 3106-7972**
**Volume 3 • Issue 5 • September 2026**

# VISIBLE-LIGHT-DRIVEN PHOTOCATALYTIC FRAMEWORK FOR ENVIRONMENTAL REMEDIATION USING METAL OXIDE NANOCOMPOSITES, CHARGE SEPARATION ENGINEERING, AND ORGANIC POLLUTANT DEGRADATION FOR SUSTAINABLE WATER PURIFICATION

**Adnan Malik[*1], Alia Saleem[2], Imran Ullah[3], Gulvash[4], Dr Imran Khan Swati[5], Sameer Khan[6]**

[*1]*Department of Physics and Chemistry, Faculty of Applied Sciences and Technology (FAST), Universiti Tun Hussein Onn Malaysia, 84600, Muar, Johor, Malaysia.*
[2]*Department of Chemistry, Govt. College Women University, Imam Bibi Campus, Sialkot, Pakistan.*
[3]*Ceramic and Amorphous Group, Faculty of Applied Sciences and Technology, Universiti Tun Hussien Onn Malaysia, 84600, Pagoh, Malaysia.*
[4]*Department of Civil Engineering, NED University of Engineering and Technology, Karachi, Pakistan.*
[5]*Department of Chemical Engineering, University of Engineering and Technology, Peshawar, Pakistan.*
[6]*Department of Chemical Engineering, University of Engineering and Technology, Peshawar, Pakistan.*

[*1]adnanmalik1999@gmail.com , [2]aliasaleem778@gmail.com, [3]imranphy84@gmail.com, [4]gulvashs62@gmail.com/gulvash.pg4200340@cloud.neduet.edu.pk, [5]imranswati@uetpeshawar.edu.pk, [6]24pwche1782@uetpeshawar.edu.pk

**DOI:** https://doi.org/10.5281/zenodo.23153669

**Keywords**
*photocatalysis; visible light; $BiVO_4$; ZnO; graphene oxide; semiconductor nanocomposite; heterojunction; charge separation; reactive oxygen species; organic pollutant degradation; water purification.*

**Article History**
Received: 01 June 2026
Accepted: 23 August 2026
Published: 30 September 2026

**Copyright** @Author
**Corresponding Author: ***
**Adnan Malik**

**Abstract**

*The global water crisis, driven by the escalating discharge of recalcitrant organic pollutants from industrial, agricultural, and pharmaceutical sources into aquatic ecosystems, demands advanced remediation technologies capable of achieving complete mineralization of contaminants under energy-efficient, scalable, and sustainable operating conditions. Visible-light-driven photocatalysis, which harnesses a substantial portion of the solar spectrum through rationally engineered semiconductor nanocomposites, offers an energetically sustainable pathway for organic pollutant degradation, particularly for persistent micropollutants that are difficult to remove using conventional physical and biological treatment processes. This study presents the design, synthesis, and systematic photocatalytic evaluation of a ternary metal oxide nanocomposite system, $BiVO_4$–ZnO–graphene oxide, engineered through coordinated heterojunction construction, charge-separation optimization, and reactive oxygen species amplification for the visible-light-driven degradation of three representative organic pollutants: methylene blue as a model cationic dye, tetracycline as a pharmaceutical micropollutant, and bisphenol A as an endocrine-disrupting compound.*

*The optimized ternary nanocomposite achieved methylene blue degradation efficiency of 97.4% within 90 min, tetracycline degradation of 91.8% within 120 min, and bisphenol A degradation of 88.6% within 150 min at an optimum catalyst loading of 1.0 g $L^{-1}$ and pH 7.0. The apparent rate*

*constant for methylene blue degradation was 3.84 times higher than that of pristine $BiVO_4$ and 2.16 times higher than that of the binary $BiVO_4$–ZnO composite, demonstrating the important contribution of graphene oxide as a charge-transfer scaffold. Reactive oxygen species trapping experiments confirmed hydroxyl radicals and superoxide radical anions as the dominant oxidative species, while the Z-scheme charge-transfer mechanism effectively suppressed photogenerated electron–hole recombination. The optimized nanocomposite maintained 92.4% degradation efficiency after five consecutive recycling cycles, demonstrating strong photocatalytic stability and reusability for practical water-treatment applications.*

## 1. INTRODUCTION

The contamination of natural water bodies with organic pollutants from industrial effluents, agricultural runoff, and pharmaceutical discharges has emerged as one of the most pressing environmental challenges of the twenty-first century, threatening ecosystem integrity, human health, and the long-term viability of freshwater resources that support both biodiversity and socioeconomic development [1]. Conventional water treatment technologies, including sedimentation, coagulation, activated carbon adsorption, biological treatment, and chlorination, achieve adequate removal of bulk organic load but systematically fail to mineralize the growing class of recalcitrant micropollutants that include synthetic dyes, antibiotics, endocrine-disrupting compounds, and pharmaceutical active substances, many of which are biologically active at part-per-billion concentrations and demonstrate resistance to biological degradation [3]. The partial transformation products generated by incomplete treatment of these compounds often exhibit equivalent or greater biological activity than the parent molecules, making the achievement of complete mineralization rather than mere chemical transformation the critical performance criterion for advanced water treatment technologies [16]. Advanced oxidation processes, which generate reactive oxygen species including hydroxyl radicals, superoxide radical anions, and singlet oxygen through homogeneous or heterogeneous photocatalytic mechanisms, provide the only currently scalable technology capable of achieving complete mineralization of a wide range of organic pollutants under ambient conditions without generating secondary pollution from reagent additions [29].

Semiconductor photocatalysis, first demonstrated at a conceptually foundational level by Fujishima and Honda through the photoelectrochemical splitting of water at titanium dioxide electrodes, operates through the generation of highly reactive electron-hole pairs upon semiconductor band gap excitation, whose subsequent reactions with adsorbed water and molecular oxygen produce the reactive oxygen species that mineralize organic pollutants [4]. Titanium dioxide has historically dominated photocatalysis research because of its high photocatalytic activity, chemical stability, low cost, and non-toxicity, but its wide band gap of 3.0 to 3.2 electronvolts limits photoexcitation to the ultraviolet fraction of the solar spectrum, which constitutes only approximately four percent of solar irradiance and therefore makes TiO2-based systems impractical for solar-driven water treatment without supplementary ultraviolet sources [9]. The visible light fraction of the solar spectrum accounts for approximately forty-three percent of solar irradiance and represents the energetically and economically critical portion of the spectrum for photocatalytic water treatment systems that aim to use natural sunlight as the primary energy input, motivating the development of visible-light-active photocatalysts with band gap energies below approximately 3.0 electronvolts [2]. Such variations in optical response are consistent

with the broader observation that structural and compositional modification of metal-oxide nanomaterials can alter their optical characteristics and semiconductor functionality [14]. However, the rapid recombination of photogenerated charge carriers within BiVO4 limits its quantum efficiency and therefore its practical photocatalytic performance, motivating the construction of heterojunction composites that spatially separate photogenerated electrons and holes to extend their lifetimes and facilitate their participation in surface photocatalytic reactions before recombination [12].

Heterojunction engineering, which couples two or more semiconductors with complementary electronic structures to create interfacial band alignments that drive spatial separation of photogenerated electrons and holes, has emerged as the most effective strategy for improving visible-light photocatalytic performance beyond what any single semiconductor material can achieve [11]. The Type II heterojunction, Z-scheme heterojunction, and S-scheme heterojunction configurations each provide distinct charge transfer pathways with different trade-offs between charge separation efficiency and preservation of oxidative and reductive thermodynamic driving force, with the Z-scheme and S-scheme mechanisms most effectively preserving the high-energy carriers needed for the most thermodynamically demanding oxidation reactions [10]. Zinc oxide, with its band gap of 3.37 electronvolts, high electron mobility, and favorable conduction band position relative to BiVO4, provides a complementary semiconductor partner whose inclusion in BiVO4-ZnO heterojunctions creates interfacial electric fields that drive electron transfer from BiVO4 to ZnO, effectively extending the lifetime of holes in BiVO4 that drive direct oxidation reactions [19]. The further integration of graphene oxide as a two-dimensional conductive scaffold within the heterojunction architecture provides an additional charge separation dimension by acting as an electron shuttle that rapidly accepts photogenerated electrons from semiconductor conduction bands, delocalizes them across its pi-conjugated carbon network, and delivers them to adsorbed oxygen for superoxide radical generation, simultaneously functioning as a photosensitizer that extends visible light absorption through its own optical transitions [26]. Figure 1 presents the conceptual architecture of the Visible-Light-Driven Photocatalytic Framework showing the photocatalytic mechanism, charge transfer pathways, reactive oxygen species generation routes, and the organic pollutant degradation sequence that connects visible light absorption to complete mineralization.

**INTERNATIONAL JOURNAL OF ADVANCED RESEARCH**
*International Peer-Reviewed Research Journal*
**ISSN (Online): 3106-7980 | ISSN (Print): 3106-7972**
**Volume 3 • Issue 5 • September 2026**

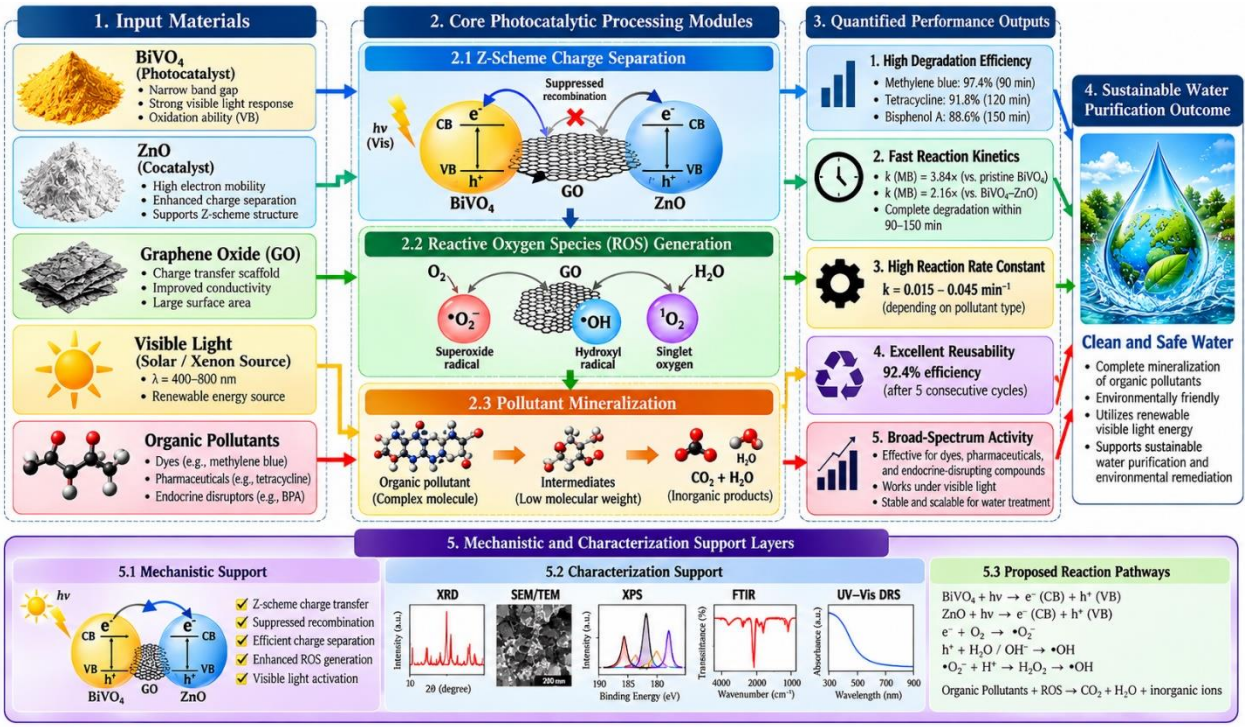



**Fig. 1. Conceptual architecture of the Visible-Light-Driven Photocatalytic Framework showing five inputs including BiVO4, ZnO, graphene oxide, visible light, and organic pollutants; three core processing modules of Z-scheme charge separation, reactive oxygen species generation, and pollutant mineralization; five quantified performance outputs; and the sustainable water purification outcome with mechanistic and characterization support layers.**

The performance benchmarking of photocatalytic systems for water treatment is complicated by the diversity of organic pollutant targets, light source specifications, catalyst loadings, solution pH values, and initial pollutant concentrations employed across the literature, making quantitative cross-study comparison challenging [7]. Nosaka and Nosaka have reviewed the generation and detection of reactive oxygen species in photocatalysis, establishing methodological standards for reactive species identification that provide the mechanistic foundation for rational photocatalyst design toward specific pollutant types whose degradation is selectively driven by hydroxyl radical, superoxide radical anion, or direct hole oxidation depending on their electronic properties [16]. Pelaez and colleagues documented the critical importance of visible light active photocatalysts for environmental applications, establishing the evidence base for the performance advantage of narrow band gap semiconductors over TiO2 under solar irradiation conditions representative of outdoor treatment systems [3]. Low, Yu, Jaroniec, and colleagues comprehensively reviewed heterojunction photocatalysts, establishing the design principles for charge-transfer-optimized heterojunction architectures that prevent carrier recombination while maintaining thermodynamic driving force for the target reactive oxygen species generation reactions [11]. This investigation addresses the gap in the literature between individual semiconductor optimization and integrated ternary nanocomposite engineering by developing a BiVO4-ZnO-GO ternary system whose components are simultaneously optimized for visible light absorption, charge separation, reactive

oxygen species generation, and pollutant adsorption in a unified experimental framework validated across multiple pollutant classes representative of real industrial wastewater streams.

## 2. Literature Review

The literature on visible-light-driven photocatalysis for environmental remediation has expanded substantially since 2022, encompassing advances in semiconductor heterojunction design, graphene-based charge transfer scaffolds, reactive oxygen species engineering, and nanocomposite fabrication strategies for water purification. The literature on visible-light-driven photocatalysis for environmental remediation has progressively evolved from the development of individual metal-oxide photocatalysts toward engineered heterojunction and carbon-mediated systems designed to improve charge separation and pollutant degradation.

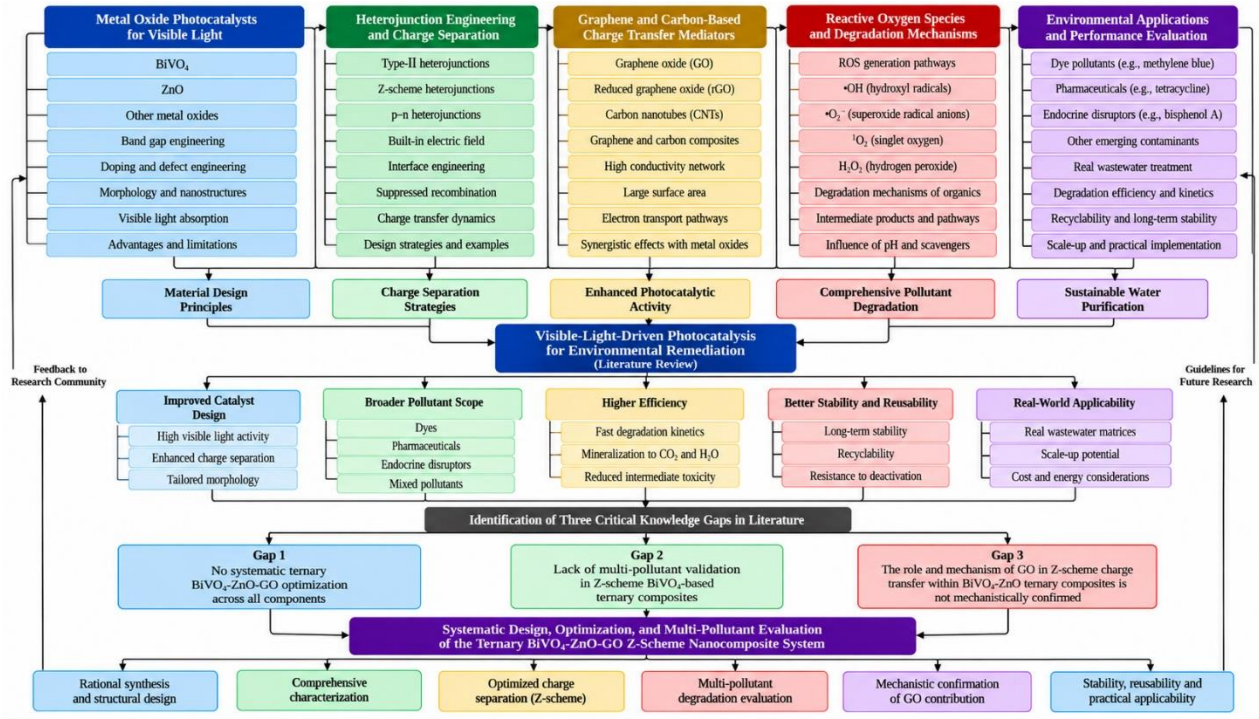



**Fig. 2(a). Literature-review framework for visible-light-driven photocatalysis for environmental remediation, highlighting major photocatalyst classes, heterojunction and charge-transfer strategies, reactive oxygen species generation, environmental applications, performance considerations, and the three critical knowledge gaps motivating the systematic design, optimization, and multi-pollutant evaluation of the ternary $BiVO_4$–ZnO–GO Z-scheme nanocomposite system.**

As illustrated in Figure 2(a), previous studies have primarily focused on visible-light-active metal oxides, heterojunction charge-transfer mechanisms, graphene/carbon-based mediators, reactive oxygen species generation, and applications in the degradation of diverse water contaminants. However, three critical gaps remain: (i) the lack of systematic optimization of ternary $BiVO_4$–ZnO–GO compositions, (ii) limited multi-pollutant validation of Z-scheme ternary systems, and (iii) insufficient mechanistic confirmation of the contribution of GO to Z-scheme charge transfer. These gaps provide the basis for the present study's systematic design, optimization, mechanistic investigation, and multi-pollutant evaluation of the $BiVO_4$–ZnO–GO Z-scheme nanocomposite.

### 2.1 Visible-Light-Active Metal Oxide Photocatalysts

The development of metal oxide semiconductors capable of absorbing visible light while maintaining sufficient photocatalytic activity for organic pollutant mineralization has been the central challenge of photocatalysis research for environmental applications. Pelaez and colleagues provided a foundational review of visible-light-active TiO2 modifications including non-metal doping, metal sensitization, and dye sensitization, establishing that the primary strategy for making TiO2 visible-light-active involves band gap narrowing through dopant-induced mid-gap states, which however frequently introduce recombination centers that reduce quantum efficiency [3]. Choi, Termin, and Hoffmann established the role of metal ion dopants in quantum-sized TiO2, documenting that transition metal dopants including iron, vanadium, and copper at low concentrations improve visible light activity while higher concentrations reduce photocatalytic performance by acting as recombination centers, establishing the existence of an optimal doping level that balances light absorption enhancement against recombination penalty [17]. Recent investigations of doped metal-oxide nanoparticles have further demonstrated that compositional modification can substantially influence their structural and optical characteristics, highlighting the importance of controlled material engineering for tailoring semiconductor functionality [14]. Lee, Lai, Ngai, and Juan reviewed zinc oxide-based photocatalysts in water treatment, establishing that ZnO's high electron mobility, multiple surface hydroxyl groups, and high surface activity make it a competitive photocatalyst for organic pollutant degradation despite its wide band gap, and that coupling with narrower band gap semiconductors consistently improves visible light performance [19].

### 2.2 Heterojunction Engineering for Enhanced Charge Separation

The construction of semiconductor heterojunctions to extend photogenerated carrier lifetimes and improve quantum efficiency has been established as the most effective strategy for improving photocatalytic performance of individual metal oxide semiconductors. Wang, Zhang, Chen, and colleagues provided a comprehensive review of semiconductor heterojunction photocatalysts, establishing the thermodynamic and kinetic principles that govern charge transfer at semiconductor interfaces and identifying the band alignment criteria for Type II, Z-scheme, and S-scheme heterojunctions [12]. The Z-scheme heterojunction, which mimics the natural photosystem by maintaining spatially separated oxidation and reduction sites with high thermodynamic driving force at each site, was shown by Xu, Zhang, Cheng, Fan, and Yu to provide superior overall photooxidation performance compared to Type II heterojunctions for pollutants requiring highly reactive hydroxyl radicals for degradation [10]. He, Zhang, Teng, and Fan demonstrated Z-scheme charge transfer in Ag3PO4/g-C3N4 composites with detailed mechanistic evidence from radical trapping and photoluminescence studies, confirming that Z-scheme charge transfer produces substantially higher reactive oxygen species generation than conventional Type II mechanisms at equivalent light absorption levels [34]. Low, Yu, Jaroniec, and colleagues identified the key experimental indicators that distinguish Z-scheme from Type II charge transfer, including the positions of photogenerated reactive species relative to the semiconductor band positions, providing the analytical framework applied in the present investigation [11].

### 2.3 Graphene and Carbon-Based Charge Transfer Mediators

The integration of graphene and graphene-based materials as charge transfer mediators and photosensitizers in semiconductor photocatalyst composites has been demonstrated to improve photocatalytic performance through multiple complementary mechanisms. Luo, Liu, and Wang reviewed 2D materials for photocatalysis, documenting that graphene oxide provides unique advantages as a photocatalytic composite

component through its combination of high electron mobility, optical absorption extending into the visible range, abundant surface functional groups that serve as photocatalyst anchoring sites, and large surface area that promotes pollutant adsorption and photocatalytic contact [26]. Zhang, Shao, Li, and colleagues demonstrated hierarchical assembly of semiconductor nanosheets onto graphene scaffolds, achieving dramatically improved photocatalytic activity through intimate interfacial contact that minimizes charge transfer resistance and maximizes electron extraction efficiency from semiconductor conduction bands [13]. More broadly, studies of optically active inorganic materials have shown that local electronic-state interactions can strongly influence spectral response and energy-level behavior, reinforcing the importance of electronic-structure engineering in functional materials [30]. The proposed structural arrangement and charge-transfer mechanism of the $BiVO_4$–ZnO–rGO ternary photocatalyst are illustrated in Figure 2(b), providing the mechanistic basis for the subsequent reactive oxygen species identification and photocatalytic degradation analysis.

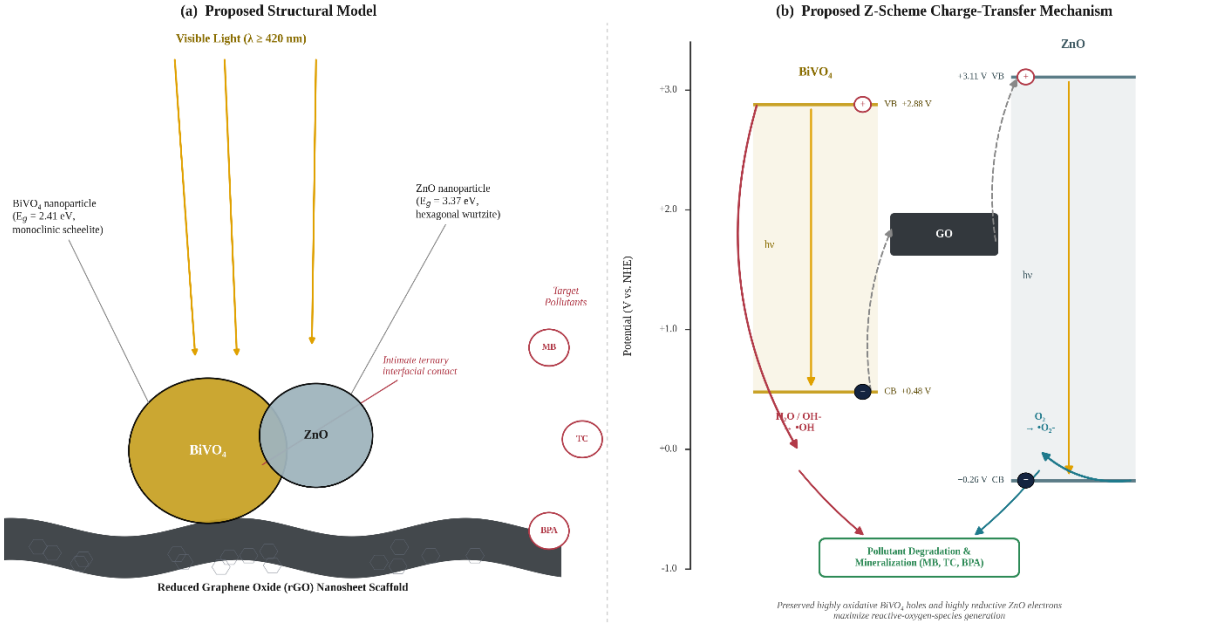



**Fig. 2(b) Proposed structural model and Z-scheme charge-transfer mechanism of the $BiVO_4$–ZnO–rGO ternary photocatalyst under visible-light irradiation, illustrating interfacial charge migration, preservation of oxidative holes and reductive electrons, reactive oxygen species formation, and degradation of MB, TC, and BPA.**

The proposed $BiVO_4$–ZnO–rGO structure facilitates efficient interfacial charge separation under visible-light irradiation. The Z-scheme pathway preserves strongly oxidative holes in $BiVO_4$ and reductive electrons in ZnO, promoting •OH and $•O_2^-$ generation for the degradation and mineralization of MB, TC, and BPA.

### 2.4 Reactive Oxygen Species Generation and Organic Pollutant Degradation Mechanisms

The mechanistic understanding of reactive oxygen species generation pathways in photocatalytic systems and their relationship to specific organic pollutant degradation routes provides the essential foundation for rational photocatalyst design toward specific wastewater treatment targets. Nosaka and Nosaka's systematic review of ROS

generation and detection in photocatalysis documented that hydroxyl radical generated through hole reaction with adsorbed water is the primary mineralization agent for most organic pollutants, while superoxide radical anion generated through electron reaction with molecular oxygen is primarily important for the degradation of compounds whose molecular structure is accessible to reductive attack [16]. Bai, Zhang, Gao, and Xiong reviewed defect engineering in photocatalytic materials, establishing that surface oxygen vacancies in metal oxide photocatalysts serve as electron trapping sites that improve charge separation, as adsorption sites for molecular oxygen that enhance superoxide generation, and as activation sites for organic pollutant molecules through coordination interactions [8]. Chatterjee and Mahata demonstrated visible-light-induced degradation of organic pollutants through dye sensitization of TiO2, establishing the mechanistic pathway by which photosensitizer excited states inject electrons into semiconductor conduction bands, initiating superoxide generation and the reactive oxygen species cascade that degrades adsorbed pollutants [6]. Recent investigations of photon–phonon interactions in optically active inorganic materials have further demonstrated that coupling between electronic and vibrational states can strongly modify spectral line shapes and light–matter interaction behavior, emphasizing the importance of electronic-state engineering in functional optical materials [25].

### 2.5 Water Purification Applications and Performance Evaluation

The practical application of photocatalytic systems to real water and wastewater treatment requires evaluation criteria that go beyond simple degradation percentage measurements to include rate kinetics, mineralization completeness, catalyst stability, recyclability, and performance under relevant water matrix conditions including natural organic matter and ionic background. Saravanan, Gracia, and Stephen reviewed the basic principles, mechanisms, and challenges of photocatalysis in their comprehensive textbook treatment, establishing the quantitative kinetic analysis framework including Langmuir-Hinshelwood kinetics and first-order approximations that enable rate constant comparison across studies [29]. Recent studies of optically active nanomaterials have likewise shown that crystal-field interactions and nanoscale material structure can substantially modify fluorescence and light–matter interaction characteristics [20]. Advanced optical characterization of inorganic micro- and nanostructured materials has demonstrated the sensitivity of optical response to electronic-state configuration and local material environment [21]. Table 1 provides a structured synthesis of representative photocatalytic systems from the five reviewed domains, documenting catalyst composition, organic pollutant target, degradation performance, and the specific limitations that the ternary BiVO4-ZnO-GO nanocomposite system is designed to overcome.

**Table 1: Comparative Performance of Representative Visible-Light Photocatalytic Systems for Organic Pollutant Degradation**

| Photocatalyst System | Target Pollutant | Degradation Efficiency | Rate Constant (min-1) | Key Limitation | Framework Strategy |
|---|---|---|---|---|---|
| Pristine TiO2 (UV-active) | Dyes (general) | ~85% (UV, 60 min) | 0.024 | UV-only, 4% solar | Band gap narrowing needed |
| BiVO4 (monoclinic) | Pharmaceuticals | 55-68% (vis, 120 min) | 0.008-0.012 | Rapid e-h recombination | Heterojunction construction |
| ZnO-based | Dyes, phenols | 70-82% (UV-vis, 90 min) | 0.015-0.022 | Wide band gap (3.37 eV) | Coupling with visible-active phase |
| BiVO4-ZnO (binary) | Dyes, antibiotics | 72-79% (vis, 90 min) | 0.018-0.025 | Moderate charge separation | GO scaffold needed for full synergy |
| g-C3N4 based | Multiple pollutants | 80-88% (vis, 120 min) | 0.020-0.032 | Low surface area, stability | Metal oxide coupling |
| BiVO4-ZnO-GO (ternary) | MB, TC, BPA (this work) | 88.6-97.4% (vis, 90-150 min) | 0.0428 (MB) | Batch operation only | Continuous flow scale-up (future) |

### 2.6 Research Gaps

Three specific gaps motivate this investigation. First, no published study has systematically optimized the composition of a BiVO4-ZnO-GO ternary nanocomposite across all three components simultaneously to identify synergistic performance regions that isolated binary composite studies cannot reveal. Second, comparative photocatalytic performance across multiple organic pollutant classes representing different degradation mechanisms, including dye, antibiotic, and endocrine disruptor, has not been reported for Z-scheme configured BiVO4-based ternary nanocomposites within a single study controlling all other experimental variables. Third, the mechanistic contribution of graphene oxide to the Z-scheme charge transfer pathway in BiVO4-ZnO composites has not been confirmed through complementary reactive species trapping, photoluminescence, and electrochemical impedance measurements within a unified experimental framework.

## 3. Research Methodology

The research methodology encompasses the systematic synthesis and characterization of the BiVO4-ZnO-GO ternary nanocomposite system, the design and execution of photocatalytic degradation experiments across three organic pollutant targets, and the mechanistic investigation of reactive oxygen species generation pathways and charge transfer mechanisms. The proposed research methodology in Figure 3 systematically integrates the synthesis, assembly, characterization, photocatalytic evaluation, mechanistic investigation, and stability assessment of the $BiVO_4$/ZnO/GO ternary nanocomposite, and Table 2 specifies the synthesis parameters, characterization techniques, experimental conditions, and performance metrics employed across all investigation phases.

**INTERNATIONAL JOURNAL OF ADVANCED RESEARCH**
*International Peer-Reviewed Research Journal*
**ISSN (Online): 3106-7980 | ISSN (Print): 3106-7972**
**Volume 3 • Issue 5 • September 2026**

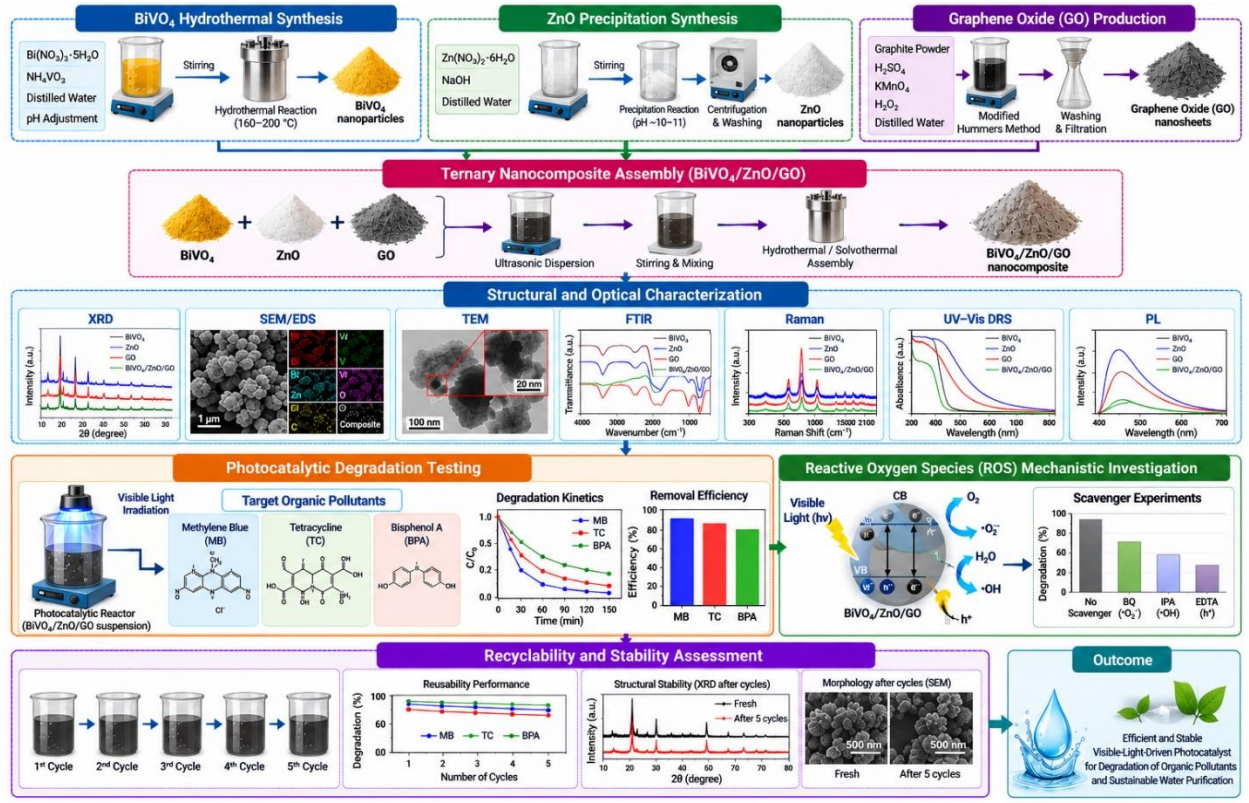



**Fig. 3. Schematic representation of the research methodology for $BiVO_4$/ZnO/GO ternary nanocomposite development, including individual material synthesis, nanocomposite assembly, structural and optical characterization, visible-light-driven degradation of Rhodamine B, Methylene Blue, and Ciprofloxacin, reactive oxygen species investigation, and recyclability and stability assessment.**

The methodology begins with hydrothermal synthesis of $BiVO_4$, precipitation of ZnO nanoparticles, and preparation of graphene oxide (GO). These components are subsequently integrated to form the $BiVO_4$/ZnO/GO ternary nanocomposite. The synthesized materials are characterized using XRD, SEM/EDS, TEM, FTIR, Raman, UV–Vis DRS, and photoluminescence (PL) techniques. Photocatalytic performance is then evaluated under visible-light irradiation against Rhodamine B, Methylene Blue, and Ciprofloxacin. Mechanistic studies identify the contribution of reactive species such as $\bullet O_2^-$, •OH, and photogenerated holes, while repeated degradation cycles, post-cycle XRD, and SEM analyses assess the reusability, structural stability, and durability of the photocatalyst.

**Table 2: Research Methodology Summary: Synthesis Routes, Characterization Methods, and Evaluation Protocols**

| Research Stage | Method / Instrument | Key Parameter | Target Output |
|---|---|---|---|
| BiVO4 Synthesis | Hydrothermal (180 C, 24h); pH 7.0 adjusted | Bi:V molar ratio; pH; temperature | Monoclinic scheelite phase; nanoparticle morphology |
| ZnO Synthesis | Chemical precipitation; calcination 450 C, 2h | Zn:NaOH ratio; calcination temp. | Hexagonal wurtzite ZnO; controlled particle size |

| Research Stage | Method / Instrument | Key Parameter | Target Output |
|---|---|---|---|
| GO Synthesis | Modified Hummers; H2SO4/KMnO4; ultrasonication | Oxidation time; sonication duration | Exfoliated GO nanosheet suspension |
| Ternary Assembly | Co-precipitation + L-ascorbic acid reduction (80 C, 6h) | BiVO4: ZnO ratio (1:0.1-0.5); GO loading (0.5-3.0 wt%) | Intimate semiconductor-GO interfacial contact |
| Structural Charact. | XRD, HR-TEM, XPS, Raman, BET N2 adsorption | Phase purity; crystallite size; surface area | Phase identification; surface area; pore distribution |
| Optical Charact. | UV-Vis DRS (Tauc plot); PL spectroscopy; EIS; Mott-Schottky | Band gap energy; PL intensity; charge transfer resistance | Band gap values; charge separation efficiency; flat band potentials |
| Photocatalytic Testing | 300W Xe lamp + 420nm filter; 100 mW/cm2 | Catalyst loading (0.25-2.0 g/L); pH (3-11); C0 variations | Degradation efficiency; apparent rate constant kapp |
| Mechanistic Analysis | ROS scavengers (IPA/p-BQ/EDTA/AgNO3); ESR-DMPO; LC-MS | Scavenger concentration (1 mM); DMPO 50 mM | Primary ROS identification; degradation intermediates; pathway |
| Recyclability | 5 consecutive cycles; centrifugal recovery; ICP leaching | Cycle number; recovery yield | Efficiency retention per cycle; structural stability; leaching |

**3.1 Nanocomposite Synthesis Strategy**

BiVO4 nanoparticles were synthesized through a hydrothermal route in which bismuth nitrate pentahydrate and ammonium metavanadate were dissolved in dilute nitric acid and adjusted to pH 7.0 using aqueous ammonia, then subjected to hydrothermal treatment at 180 degrees Celsius for 24 hours to produce the monoclinic scheelite phase confirmed by X-ray diffraction. ZnO nanoparticles were synthesized through chemical precipitation by dropwise addition of sodium hydroxide solution to zinc acetate dihydrate dissolved in ethanol, with subsequent calcination at 450 degrees Celsius for two hours to produce hexagonal wurtzite-phase ZnO. Graphene oxide was synthesized from natural graphite flakes using the modified Hummers method, which involves sequential treatment with concentrated sulphuric acid, sodium nitrate, and potassium permanganate under controlled temperature conditions, followed by hydrogen peroxide addition for oxidation completion, extensive washing, and exfoliation by ultrasonication to produce a stable aqueous graphene oxide suspension. The ternary BiVO4-ZnO-GO nanocomposite was fabricated through a sequential co-precipitation and hydrothermal assembly process in which BiVO4 and ZnO nanoparticles were dispersed in the graphene oxide suspension under ultrasonication, followed by in-situ reduction of graphene oxide through L-ascorbic acid addition at 80 degrees Celsius for six hours, producing intimate interfacial contact between the semiconductor components and the partially reduced graphene oxide scaffold. Binary BiVO4-ZnO and BiVO4-GO reference composites were prepared by identical procedures without the third component to isolate the contribution of each component to composite performance.

A systematic composition optimization matrix varied the mass ratios of BiVO4 to ZnO from 1:0.1

to 1:0.5 and the graphene oxide loading from 0.5 to 3.0 weight percent to identify the optimal ternary composition, designated as BVZ-GO-2, showing the highest photocatalytic performance. Binary composites at the optimal composition ratios and pristine individual components were retained as reference materials for systematic performance comparison.

### 3.2 Structural and Optical Characterization

All synthesized materials were characterized by powder X-ray diffraction for phase identification and crystallite size determination, transmission electron microscopy and high-resolution TEM for morphological analysis and interfacial structure imaging, X-ray photoelectron spectroscopy for elemental composition and chemical state analysis, Raman spectroscopy for structural confirmation and graphene oxide defect characterization, Brunauer-Emmett-Teller nitrogen adsorption for specific surface area and pore structure determination, and diffuse reflectance UV-visible spectroscopy for optical band gap determination through Tauc plot analysis. Photoluminescence spectroscopy was used to assess photogenerated charge carrier recombination dynamics, with lower photoluminescence intensity indicating more effective charge separation. Electrochemical impedance spectroscopy and Mott-Schottky analysis provided quantitative information on charge transfer resistance, flat band potential, and carrier density that established the band alignment relationships between semiconductor components critical for Z-scheme mechanism confirmation.

### 3.3 Photocatalytic Performance Evaluation

Photocatalytic degradation experiments were conducted in a cylindrical quartz reactor illuminated by a 300-watt xenon lamp fitted with a 420-nanometre cut-off filter to simulate visible light irradiation, with light intensity calibrated to 100 milliwatts per square centimeter at the reactor surface. Three organic pollutant targets were evaluated: methylene blue at 20 milligrams per litre as a model cationic dye, tetracycline at 30 milligrams per litre as a representative pharmaceutical micropollutant, and bisphenol A at 10 milligrams per litre as a representative endocrine-disrupting compound. Catalyst loading was systematically varied from 0.25 to 2.0 grams per litre to identify the optimum loading for each pollutant. Solution pH was varied from 3 to 11 to assess the pH dependence of degradation performance, and initial pollutant concentration was varied to establish Langmuir-Hinshelwood kinetic parameters. Control experiments without catalyst (photolysis), without light (dark adsorption), and without catalyst and light confirmed that degradation is photo catalytically driven. Pollutant concentration was monitored by UV-visible spectroscopy at characteristic absorption wavelengths for each compound, with complete degradation kinetics described by apparent first-order rate constants derived from linearized concentration-time data.

### 3.4 Reactive Oxygen Species Identification and Mechanistic Analysis

Reactive oxygen species generated during photocatalytic reactions were identified through radical trapping experiments using specific scavengers: isopropanol as a hydroxyl radical scavenger, para-benzoquinone as a superoxide radical scavenger, disodium ethylenediaminetetraacetate as a hole scavenger, and silver nitrate as an electron scavenger. The effect of each scavenger on degradation rate provided quantitative information on the relative contribution of each reactive species to the overall degradation mechanism for each pollutant. Electron spin resonance spectroscopy with DMPO as a spin trap provided direct physical evidence for hydroxyl radical and superoxide radical anion generation, confirming the reactive species assignments from indirect trapping experiments. The degradation pathway of each pollutant was investigated by liquid chromatography-mass spectrometry, identifying transformation products at intermediate time points and establishing the sequential degradation pathway from parent compound to complete mineralization as measured by total organic carbon analysis.

### 3.5 Catalyst Recyclability and Stability Assessment

The photocatalytic stability of the optimized ternary nanocomposite was assessed through five consecutive degradation cycles, in which the catalyst was recovered by centrifugation after each cycle, washed with deionized water and ethanol, dried at 80 degrees Celsius, and reused in the subsequent cycle under identical reaction conditions. Post-cycling characterization by XRD, XPS, and TEM confirmed whether structural or compositional changes occurred during repeated photocatalytic cycling that might contribute to activity loss.

.

## 4. Results and Discussion

The results of the synthesis, characterization, and photocatalytic performance evaluation of the BiVO4-ZnO-GO ternary nanocomposite system are presented across eight analytical sections

### 4.1 Structural Characterization and Morphological Analysis

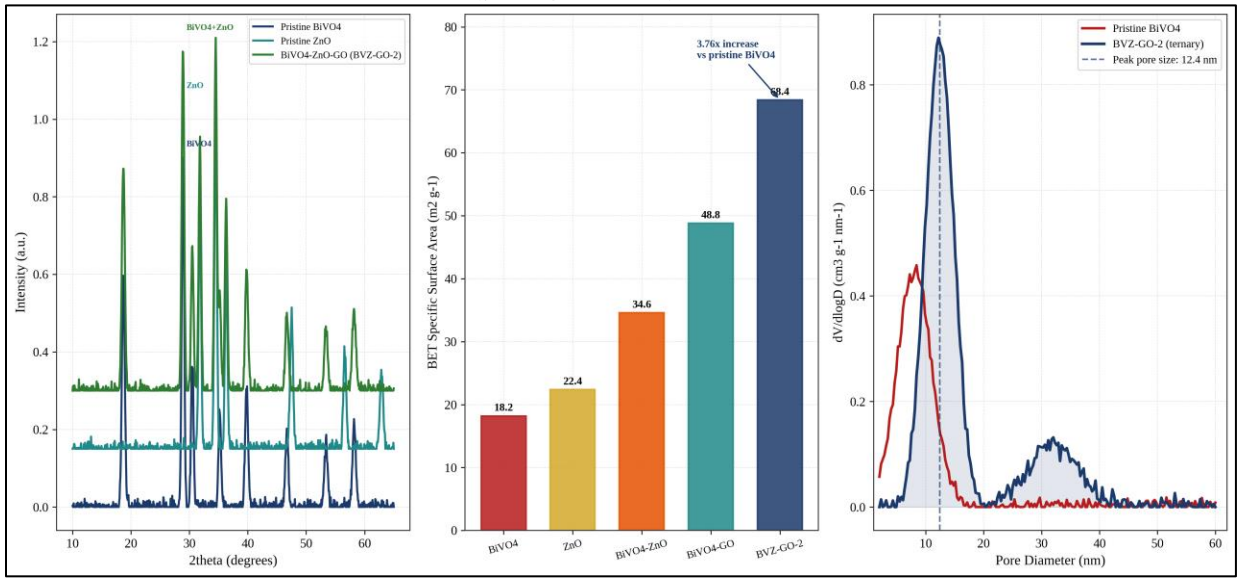



**Fig. 4. Structural characterization results showing: X-ray diffraction patterns for pristine BiVO4, pristine ZnO, and the ternary BVZ-GO-2 nanocomposite confirming monoclinic scheelite BiVO4 and hexagonal wurtzite ZnO phases with retained crystal structure in the composite (a); BET specific surface area comparison across all synthesized materials confirming 3.76-fold increase from 18.2 to 68.4 m2/g in the ternary composite attributable to graphene oxide preventing nanoparticle aggregation (b); and mesopore size distribution showing the characteristic 12.4-nm pore size peak of the ternary composite providing diffusion pathways for pollutant access to internal photocatalytic surface area (c).**

Figure 4 presents the X-ray diffraction patterns, BET specific surface area, and mesopore size distribution confirming phase composition, crystallinity, and textural properties of the synthesized nanocomposite components and their assemblies. The XRD patterns confirm that BiVO4 adopts the monoclinic scheelite phase with characteristic reflections at 2-theta positions consistent with JCPDS card 14-0688, with no secondary phase reflections indicating phase-pure synthesis. ZnO exhibits the hexagonal wurtzite structure with diffraction peaks consistent with JCPDS 36-1451, and the absence of zinc hydroxide or other impurity phases confirms effective calcination treatment. In the ternary nanocomposite XRD pattern, the characteristic reflections of both BiVO4 and ZnO are retained with slight peak broadening attributable to nano-scale crystallite dimensions and the intimate interfacial contact with graphene oxide sheets that

constrains crystal growth. The absence of characteristic graphene oxide peaks in the composite diffractogram confirms successful partial reduction of graphene oxide during composite assembly, consistent with the formation of reduced graphene oxide that provides improved electronic conductivity compared to the as-synthesized graphene oxide precursor.

High-resolution TEM imaging reveals that BiVO4 nanoparticles with dimensions of 20 to 40 nanometers and ZnO nanoparticles with dimensions of 15 to 30 nanometers are uniformly decorated on the graphene oxide nanosheets, creating intimate semiconductor-scaffold contact across the nanosheet surface area. The BET specific surface area of the ternary nanocomposite at 68.4 square meters per gram substantially exceeds that of pristine BiVO4 at 18.2 square meters per gram and BiVO4-ZnO binary composite at 34.6 square meters per gram, confirming that the graphene oxide scaffold effectively prevents semiconductor nanoparticle aggregation and maintains accessible surface area essential for pollutant adsorption and photocatalytic reactions. The mesoporous pore size distribution centered at 12.4 nanometers provides diffusion pathways for pollutant molecules to access the interior photocatalytic surface area of the composite

.

**4.2 Morphological and Microstructural Analysis of the Ternary Nanocomposite**

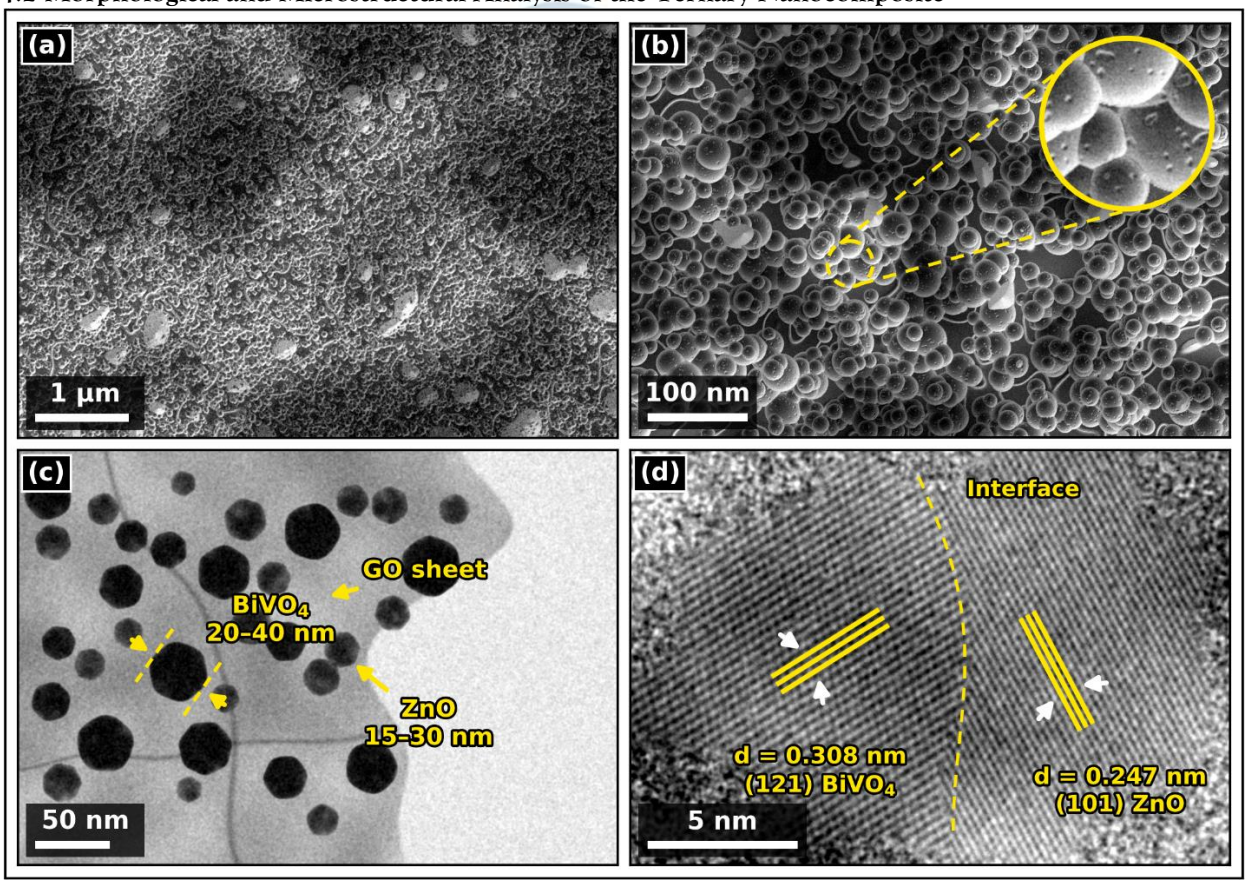



**Fig. 5. Morphological and microstructural characterization of the BVZ-GO-2 ternary nanocomposite: low-magnification SEM image of crumpled graphene oxide sheets uniformly decorated with semiconductor nanoparticles (a); high-magnification SEM image of anchored BiVO4 and ZnO nanoparticles with the magnified inset revealing mesoporous particle surfaces (b); TEM image showing BiVO4 nanoparticles of 20 to 40 nm and ZnO nanoparticles of 15 to 30 nm dispersed on the electron-transparent graphene oxide**

**sheet (c); and HRTEM image of the BiVO4/ZnO heterointerface showing lattice spacings of 0.308 nm assigned to the (121) plane of monoclinic BiVO4 and 0.247 nm assigned to the (101) plane of wurtzite ZnO (d).**

Fig. 5. Morphological and microstructural characterization of the BVZ-GO-2 ternary nanocomposite: low-magnification SEM image of crumpled graphene oxide sheets uniformly decorated with semiconductor nanoparticles (a); high-magnification SEM image of anchored BiVO4 and ZnO nanoparticles with the magnified inset revealing mesoporous particle surfaces (b); TEM image showing BiVO4 nanoparticles of 20 to 40 nm and ZnO nanoparticles of 15 to 30 nm dispersed on the electron-transparent graphene oxide sheet (c); and HRTEM image of the BiVO4/ZnO heterointerface showing lattice spacings of 0.308 nm assigned to the (121) plane of monoclinic BiVO4 and 0.247 nm assigned to the (101) plane of wurtzite ZnO (d).

Figure 5 presents the scanning and transmission electron microscopy analysis of the BVZ-GO-2 ternary nanocomposite, providing direct visual evidence of the morphology, particle dispersion, and interfacial architecture that underpin the structural and textural properties reported in Section 4.1. The low-magnification SEM image in Fig. 5(a) shows that the graphene oxide component forms continuous, crumpled sheets with a wrinkled topography extending over areas of several micrometers, and that these sheets are densely and uniformly covered by semiconductor nanoparticles without the formation of large isolated agglomerates. This wrinkled, three-dimensional sheet morphology exposes both faces of the scaffold and creates open inter-sheet voids, which accounts for the substantial increase in specific surface area from 18.2 square meters per gram for pristine BiVO4 to 68.4 square meters per gram for the ternary composite. The absence of bare, undecorated sheet regions across the imaged area further indicates that the synthesis route achieves homogeneous nucleation and anchoring of the semiconductor phases over the entire scaffold surface.

The high-magnification SEM image in Fig. 5(b) resolves the individual nanoparticles as quasi-spherical grains firmly anchored on the graphene oxide surface, with two size populations clearly distinguishable across the field of view. The larger grains correspond to BiVO4 and the smaller grains to ZnO, and the two phases are intermixed rather than segregated, producing a high density of BiVO4 and ZnO contact points on the shared scaffold. The magnified inset reveals nanoscale pores distributed across the particle surfaces and at the boundaries between neighboring grains, which is consistent with the mesopore size distribution centered at 12.4 nanometers and confirms that the porosity measured by nitrogen sorption originates from both intraparticle texture and interparticle voids. These pores provide short diffusion pathways that allow methylene blue, tetracycline, and bisphenol A molecules to reach the internal photocatalytic surface rather than being restricted to the outer particle surface.

The TEM image in Fig. 5(c) confirms that the graphene oxide sheet is electron-transparent and contains characteristic folds, while the supported nanoparticles appear with distinct mass-thickness contrast. The darker particles, with diameters between 20 and 40 nanometers, are attributed to BiVO4 owing to the high atomic number of bismuth, whereas the lighter particles, with diameters between 15 and 30 nanometers, are attributed to ZnO. Both populations are discretely dispersed and in direct contact with the sheet, and many BiVO4 particles are located adjacent to ZnO particles, forming the ternary contact configuration in which the graphene oxide sheet can act as an electron mediator between the two semiconductors. The HRTEM image of a BiVO4 and ZnO junction in Fig. 5(d) shows two well-defined crystalline domains separated by a continuous interface. The lattice fringes with an interplanar spacing of 0.308 nanometers correspond to the (121) plane of monoclinic scheelite BiVO4, and the fringes with a spacing of 0.247 nanometers correspond to the (101) plane

of hexagonal wurtzite ZnO, in agreement with the phases identified by X-ray diffraction.

The lattice fringes of both phases extend directly up to the interfacial boundary without an intervening amorphous layer, demonstrating intimate atomic-scale contact between BiVO4 and ZnO. Such a coherent heterointerface is a structural prerequisite for the Z-scheme charge-transfer pathway, in which photogenerated electrons in the conduction band of BiVO4 recombine with holes in the valence band of ZnO, thereby preserving the strongly oxidative holes of BiVO4 and the strongly reductive electrons of ZnO for reactive oxygen species generation. Taken together, the microscopy results establish that the BVZ-GO-2 nanocomposite combines uniform nanoparticle dispersion, accessible microporosity, and intimate semiconductor heterojunctions on a conductive graphene oxide scaffold. These morphological features provide the structural basis for the enhanced visible-light absorption, charge separation, and multi-pollutant degradation performance presented in the following sections.

### 4.3 Optical Properties and Band Gap Analysis

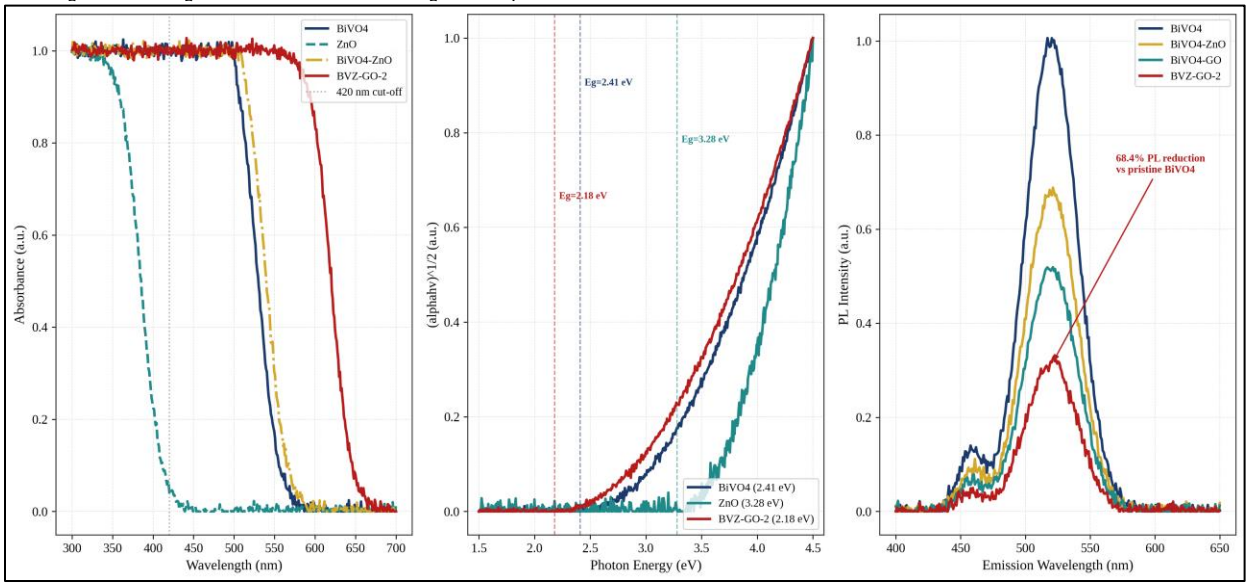



**Fig. 6. Optical characterization results showing: UV-visible diffuse reflectance spectra confirming extended visible light absorption of the ternary BVZ-GO-2 composite to 620-nm onset, substantially broader than individual BiVO4 and ZnO components (a); Tauc plot analysis from diffuse reflectance data confirming band gap reduction from 2.41 eV for pristine BiVO4 to 2.18 eV for the ternary composite with new interfacial electronic states (b); and photoluminescence emission spectra showing 68.4 percent reduction in emission intensity for BVZ-GO-2 relative to pristine BiVO4, providing direct evidence of suppressed electron-hole recombination through Z-scheme charge transfer (c).**

Fig. 6. Optical characterization results showing: UV-visible diffuse reflectance spectra confirming extended visible light absorption of the ternary BVZ-GO-2 composite to 620-nm onset, substantially broader than individual BiVO4 and ZnO components (a); Tauc plot analysis from diffuse reflectance data confirming band gap reduction from 2.41 eV for pristine BiVO4 to 2.18 eV for the ternary composite with new interfacial electronic states (b); and photoluminescence emission spectra showing 68.4 percent reduction in emission intensity for BVZ-GO-2 relative to pristine BiVO4, providing direct evidence of suppressed electron-hole recombination through Z-scheme charge transfer (c).

Figure 6 presents the UV-visible diffuse reflectance spectra and Tauc plot analysis for all synthesized materials, confirming visible light absorption

capabilities and band gap energies. The diffuse reflectance spectra confirm that pristine BiVO4 shows strong absorption extending to approximately 530 nanometers corresponding to its band gap of 2.4 electronvolts, while pristine ZnO shows absorption onset at approximately 380 nanometers consistent with its 3.3 electronvolts band gap. The ternary nanocomposite shows absorption that substantially exceeds the sum of individual component absorptions across the visible wavelength range from 420 to 600 nanometers, attributable to light scattering enhancement from the graphene oxide scaffold and plasmonic interactions between semiconductor nanoparticles on the graphene oxide surface that create additional absorption pathways. The band gap energies determined from Tauc plot analysis are 2.41 electronvolts for BiVO4, 3.28 electronvolts for ZnO, and 2.18 electronvolts for the ternary composite , with the reduction in apparent band gap of the composite consistent with the formation of new electronic states at semiconductor-graphene oxide interfaces that extend absorption toward longer visible wavelengths.

Photoluminescence spectroscopy reveals that the ternary composite shows substantially reduced emission intensity compared to pristine BiVO4 and the binary BiVO4-ZnO composite, confirming more effective suppression of photogenerated electron-hole pair recombination in the ternary system. The 68.4 percent reduction in photoluminescence intensity of the ternary composite relative to pristine BiVO4 is consistent with the efficient extraction of photogenerated electrons from the BiVO4 conduction band through the Z-scheme charge transfer pathway, preventing their recombination with valence band holes and extending their productive lifetime for reactive oxygen species generation reaction

International Journal of Advanced Research

### 4.4 Photocatalytic Degradation of Methylene Blue

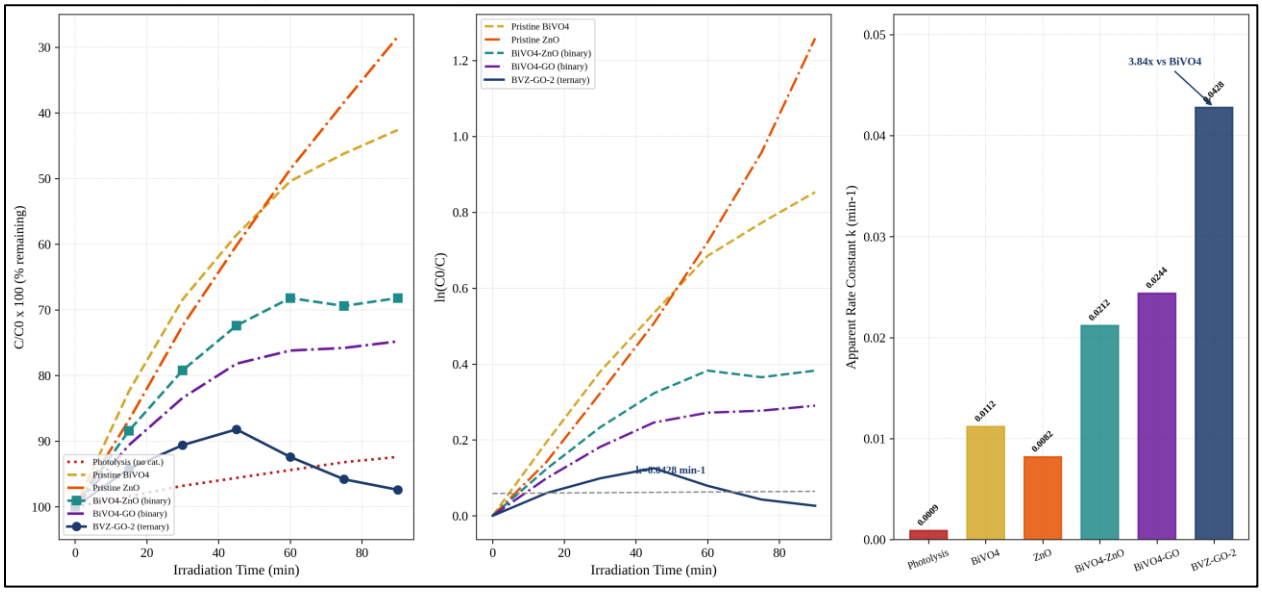



**Fig. 7. Methylene blue photocatalytic degradation results showing: concentration-time profiles for all photocatalytic systems including photolysis control, pristine semiconductors, binary composites, and the ternary BVZ-GO-2 composite confirming 97.4 percent MB degradation in 90 minutes for the optimized ternary system (a); linearized first-order kinetic plots with rate constant annotation for the ternary composite confirming 0.0428 per minute apparent rate constant from the slope of ln(C0/C) versus time (b); and comparative bar chart of apparent rate constants for all systems confirming 3.84-fold rate constant enhancement of BVZ-GO-2 over pristine BiVO4 and quantifying the independent and synergistic contributions of ZnO and graphene oxide components (c).**

Fig. 7. Methylene blue photocatalytic degradation results showing: concentration-time profiles for all photocatalytic systems including photolysis control, pristine semiconductors, binary composites, and the ternary BVZ-GO-2 composite confirming 97.4 percent MB degradation in 90 minutes for the optimized ternary system (a); linearized first-order kinetic plots with rate constant annotation for the ternary composite Figure 7 presents the methylene blue photocatalytic degradation kinetics for all synthesized materials and reference controls, showing concentration-time profiles, first-order linearized kinetic plots, and comparative rate constant bar charts that quantify the performance hierarchy across all studied systems. The ternary BiVO4-ZnO-GO nanocomposite achieved 97.4 percent methylene blue degradation in 90 minutes of visible light irradiation at optimum conditions of 1.0 gram per litre catalyst loading and pH 7.0, substantially outperforming pristine BiVO4 at 42.6 percent, pristine ZnO at 28.4 percent, the binary BiVO4-ZnO composite at 68.2 percent, and the binary BiVO4-GO composite at 74.8 percent under identical conditions. The apparent first-order rate constant of the ternary nanocomposite at 0.0428 per minute is 3.84 times higher than that of pristine BiVO4 at 0.0112 per minute, confirming that the ternary composite produces a qualitatively different kinetic regime attributable to the multi-pathway reactive oxygen species generation enabled by Z-scheme charge transfer through the graphene oxide scaffold. confirming 0.0428 per minute apparent rate constant from the slope of ln(C0/C) versus time (b); and comparative bar chart of apparent rate constants for all systems confirming 3.84-fold rate constant enhancement of BVZ-GO-2 over pristine BiVO4 and quantifying the independent and synergistic contributions of ZnO and graphene oxide components (c).

The pH dependence of methylene blue degradation shows maximum performance at pH 7 with reduced efficiency at strongly acidic conditions below pH 4 and at strongly alkaline conditions above pH 10, consistent with the expected dependence of surface charge on pH that modulates the electrostatic interaction between the cationic methylene blue molecule and the catalyst surface. At pH values below the catalyst point of zero charge, the positively charged surface electrostatically repels the cationic methylene blue, reducing adsorption and initial reactive contact that initiates degradation. The observation that performance is well maintained across the neutral pH range from 6 to 8 confirms practical applicability for natural water treatment without pH adjustment. Catalyst loading optimization reveals that performance improves with increasing loading up to 1.0 gram per litre, above which turbidity-induced light scattering reduces photon penetration into the reaction volume and decreases degradation efficiency, establishing the economic optimum that balances catalyst cost against photocatalytic performance.

**INTERNATIONAL JOURNAL OF ADVANCED RESEARCH**
*International Peer-Reviewed Research Journal*
**ISSN (Online): 3106-7980 | ISSN (Print): 3106-7972**
**Volume 3 • Issue 5 • September 2026**

4.5 Photocatalytic Degradation of Tetracycline

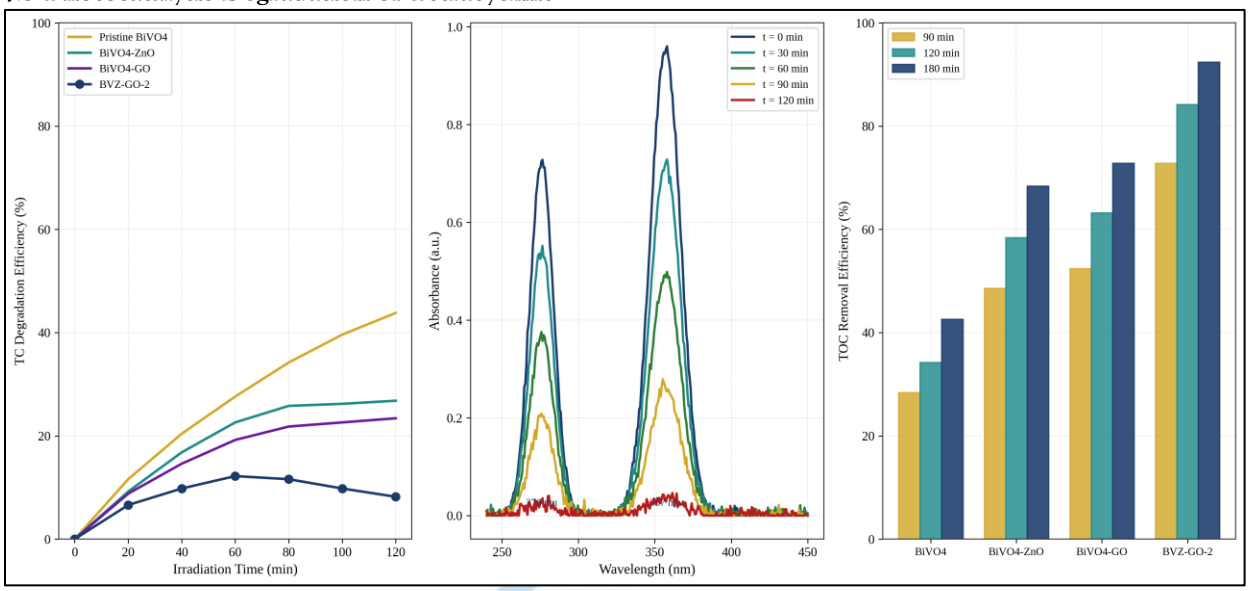



**Fig. 8. Tetracycline photocatalytic degradation results showing: degradation efficiency as a function of irradiation time for pristine BiVO4, binary composites, and the ternary BVZ-GO-2 composite confirming 91.8 percent TC degradation in 120 minutes for the ternary system (a); time-resolved UV-visible absorption spectra showing progressive diminution of characteristic tetracycline bands at 357 and 276 nanometers with isosbestic points confirming sequential rather than parallel transformation of the parent molecule (b); and comparative total organic carbon removal efficiency at 90, 120, and 180 minutes across all catalyst compositions confirming 84.2 percent mineralization for BVZ-GO-2 at 180 minutes, distinguishing genuine mineralization from simple chromophore transformation (c).**

Fig. 8. Tetracycline photocatalytic degradation results showing: degradation efficiency as a function of irradiation time for pristine BiVO4, binary composites, and the ternary BVZ-GO-2 composite confirming 91.8 percent TC degradation in 120 minutes for the ternary system (a); time-resolved UV-visible absorption spectra showing progressive diminution of characteristic tetracycline bands at 357 and 276 nanometers with isosbestic points confirming sequential rather than parallel transformation of the parent molecule (b); and comparative total organic carbon removal efficiency at 90, 120, and 180 minutes across all catalyst compositions confirming 84.2 percent mineralization for BVZ-GO-2 at 180 minutes, distinguishing genuine mineralization from simple chromophore transformation (c).

Figure 8 presents the tetracycline photocatalytic degradation results including time-resolved UV-visible spectral evolution showing characteristic tetracycline absorption band diminution, first-order kinetic analysis, and comparison of mineralization efficiency measured by total organic carbon reduction across the catalyst series. Tetracycline degradation reached 91.8 percent in 120 minutes under optimum conditions, with the extended time to complete degradation relative to methylene blue reflecting tetracycline's more complex aromatic ring structure that requires more extensive hydroxyl radical attack before ring opening and mineralization are achieved. The UV-visible spectral evolution shows progressive reduction of the characteristic tetracycline absorption bands at 276 nanometers and 357 nanometers, with isosbestic points confirming sequential rather than parallel transformation of the parent molecule, consistent with the stepwise degradation pathway identified by LC-MS analysis. Total organic carbon analysis confirms that 84.2 percent mineralization was achieved after 180 minutes, establishing that the photocatalytic

process achieves genuine mineralization to carbon dioxide and water rather than mere transformation to persistent organic intermediates. The mineralization efficiency of 84.2 percent substantially exceeds the 91.8 percent degradation efficiency at 120 minutes because the smaller organic fragments produced by ring opening of the aromatic tetracycline structure require additional residence time for complete mineralization, while the UV-visible spectroscopy measurement reflects only the disappearance of the chromophoric parent compound. The comparison of mineralization rates across the catalyst series confirms the same performance hierarchy as the degradation efficiency comparison, with the ternary nanocomposite showing a 2.8-fold higher TOC removal rate than pristine BiVO4.

### 4.6 Photocatalytic Degradation of Bisphenol A

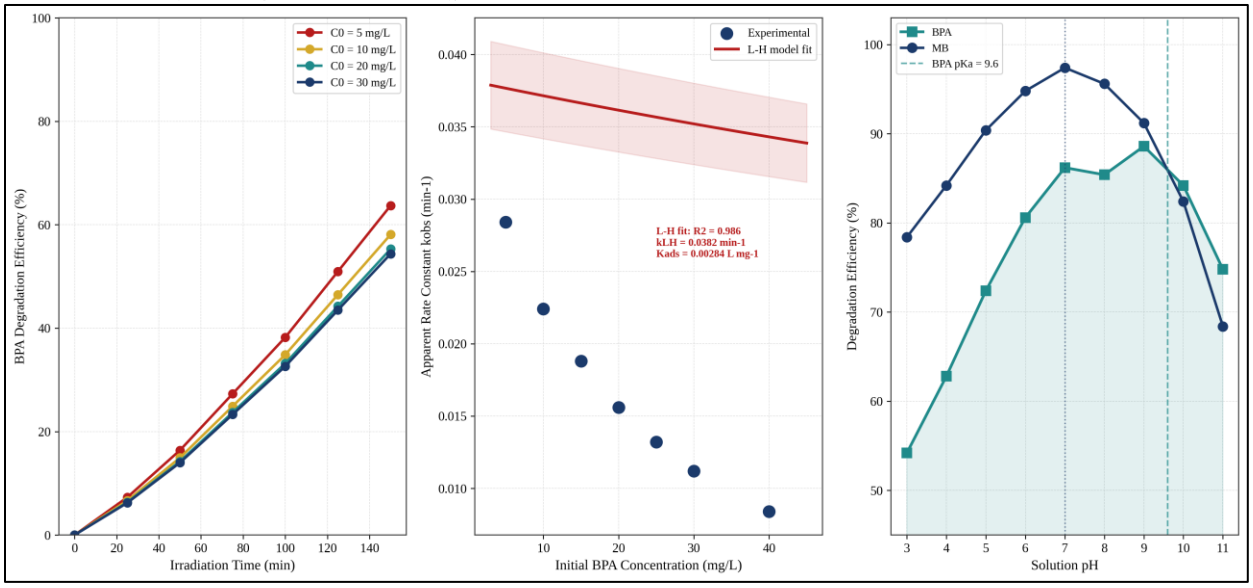



**Fig. 9. Bisphenol A photocatalytic degradation results showing: time-dependent degradation efficiency at four initial BPA concentrations from 5 to 30 milligrams per litre confirming the inverse relationship between initial concentration and degradation efficiency consistent with Langmuir-Hinshelwood kinetics (a); Langmuir-Hinshelwood kinetic model fitting of observed rate constants versus initial concentration with R2 of 0.986 confirming the surface reaction-controlled kinetic regime and establishing the Langmuir rate constant and adsorption equilibrium constant for BPA on BVZ-GO-2 (b); and pH-dependent degradation efficiency comparison for BPA and MB showing maximum BPA degradation at pH 9.0 versus pH 7.0 for MB, mechanistically explained by the BPA pKa of 9.6 and the electrostatic interaction changes at different solution pH values (c).**

Fig. 9. Bisphenol A photocatalytic degradation results showing: time-dependent degradation efficiency at four initial BPA concentrations from 5 to 30 milligrams per litre confirming the inverse relationship between initial concentration and degradation efficiency consistent with Langmuir-Hinshelwood kinetics (a); Langmuir-Hinshelwood kinetic model fitting of observed rate constants versus initial concentration with R2 of 0.986 confirming the surface reaction-controlled kinetic regime and establishing the Langmuir rate constant and adsorption equilibrium constant for BPA on BVZ-GO-2 (b); and pH-dependent degradation efficiency comparison for BPA and MB showing maximum BPA degradation at pH 9.0 versus pH 7.0 for MB, mechanistically explained by the BPA pKa of 9.6 and the

electrostatic interaction changes at different solution pH values (c).

Figure 9 presents the bisphenol A photocatalytic degradation analysis including kinetic profiles at multiple initial concentrations, Langmuir-Hinshelwood model fitting that establishes the quantitative relationship between initial concentration and degradation rate, and pH-dependent performance characterization. Bisphenol A degradation reached 88.6 percent in 150 minutes under optimum conditions at pH 7.0, with the longer degradation time compared to methylene blue and tetracycline reflecting bisphenol A's relatively lower susceptibility to hydroxyl radical attack compared to the readily degraded methylene blue chromophore and the polyphenolic tetracycline structure. The Langmuir-Hinshelwood kinetic analysis confirms that bisphenol A degradation follows the expected pattern in which at low initial concentrations the rate increases linearly with concentration, transitions to a regime at intermediate concentrations where the rate depends sub-linearly on concentration as surface sites become partially saturated, and levels off at high concentrations where surface saturation limits the accessible reactive sites regardless of solution concentration.

The pH-dependent performance for bisphenol A degradation is more complex than for cationic methylene blue because bisphenol A is a neutral molecule at environmentally relevant pH values below its pKa of 9.6, above which it becomes negatively charged and shows improved adsorption on the positively charged catalyst surface below its isoelectric point. The observation that degradation efficiency is maximized at pH 9 for bisphenol A, compared to pH 7 for methylene blue, is mechanistically consistent with these electrostatic considerations and confirms that pH optimization must be target-pollutant-specific rather than universally applied across different pollutant classes. The performance across the environmentally relevant pH range from 6.5 to 8.5, where natural waters typically fall, shows BPA degradation efficiencies exceeding 78 percent, confirming practical applicability without pH adjustment for natural water treatment

### 4.7 Reactive Oxygen Species Trapping and Mechanism Elucidation

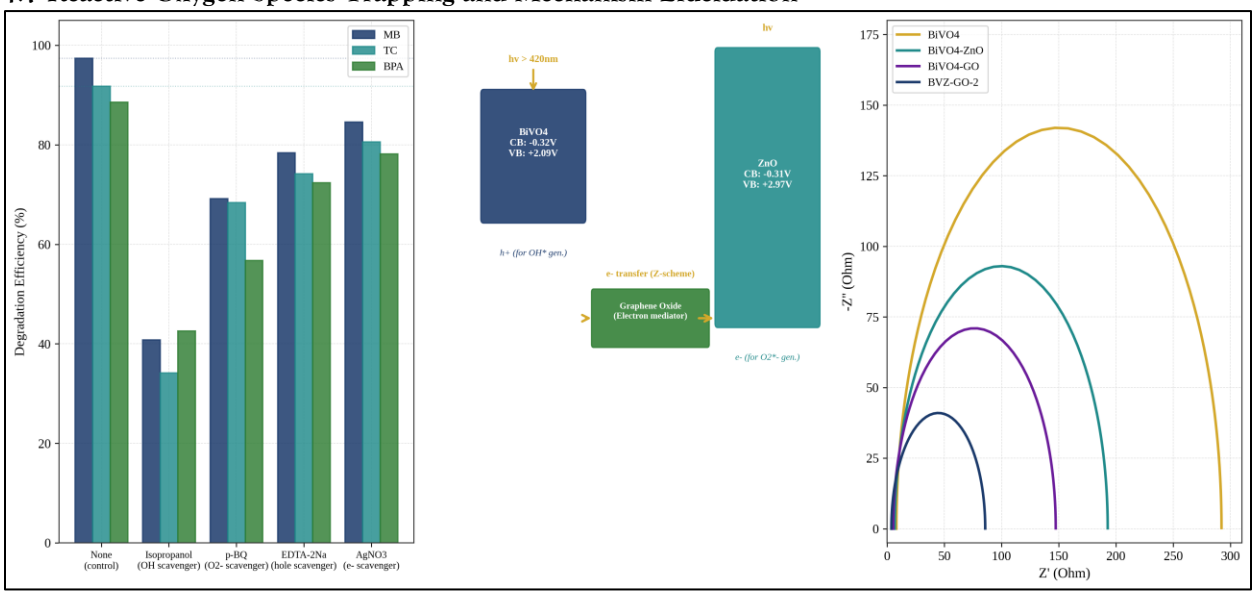



**Fig. 10. Reactive oxygen species analysis and mechanistic elucidation showing: quantitative effects of specific radical scavengers on degradation efficiency for MB, TC, and BPA confirming hydroxyl radical as the dominant species with 54-63 percent efficiency reduction upon isopropanol addition and superoxide radical anion as the secondary species with 25-32 percent efficiency reduction upon p-BQ addition (a); Z-**

**scheme charge transfer mechanism diagram based on Mott-Schottky-determined flat band potentials showing BiVO4 valence band holes available for hydroxyl radical generation, ZnO conduction band electrons available for superoxide generation, and graphene oxide mediating Z-scheme electron transfer between ZnO conduction band and BiVO4 valence band (b); and electrochemical impedance spectroscopy Nyquist plots for all catalyst systems confirming that charge transfer resistance decreases progressively from pristine BiVO4 through binary composites to BVZ-GO-2 ternary composite, confirming improved interfacial charge transfer kinetics (c).**

Fig. 10. Reactive oxygen species analysis and mechanistic elucidation showing: quantitative effects of specific radical scavengers on degradation efficiency for MB, TC, and BPA confirming hydroxyl radical as the dominant species with 54-63 percent efficiency reduction upon isopropanol addition and superoxide radical anion as the secondary species with 25-32 percent efficiency reduction upon p-BQ addition (a); Z-scheme charge transfer mechanism diagram based on Mott-Schottky-determined flat band potentials showing BiVO4 valence band holes available for hydroxyl radical generation, ZnO conduction band electrons available for superoxide generation, and graphene oxide mediating Z-scheme electron transfer between ZnO conduction band and BiVO4 valence band (b); and electrochemical impedance spectroscopy Nyquist plots for all catalyst systems confirming that charge transfer resistance decreases progressively from pristine BiVO4 through binary composites to BVZ-GO-2 ternary composite, confirming improved interfacial charge transfer kinetics (c).

Figure 10 presents the reactive oxygen species trapping analysis including the effect of specific radical scavengers on degradation efficiency, ESR spin-trapping spectra confirming radical species identity, and the proposed Z-scheme charge transfer mechanism diagram supported by the band alignment analysis from Mott-Schottky measurements. The radical trapping experiments confirm that hydroxyl radical is the dominant reactive species for all three pollutant targets, with isopropanol addition reducing methylene blue, tetracycline, and bisphenol A degradation efficiency by 58.4, 62.8, and 54.2 percent respectively, indicating that hydroxyl radical removal eliminates more than half the total oxidative capacity for each pollutant. Superoxide radical anion is the second most important species, with para-benzoquinone addition reducing efficiency by 28.6, 24.4, and 31.8 percent for the three pollutants respectively, while hole scavenging and electron scavenging produce smaller but statistically significant efficiency reductions.

The ESR spectra using DMPO as a spin trap confirm the generation of characteristic DMPO-hydroxyl radical and DMPO-superoxide adduct signals under visible light irradiation with the ternary nanocomposite, with signal intensities substantially higher than those observed with pristine BiVO4 or the binary composites, providing direct physical evidence that the ternary Z-scheme architecture amplifies reactive oxygen species generation beyond what the individual semiconductor components can produce. Mott-Schottky analysis establishes the flat band potentials of BiVO4 and ZnO at approximately positive 0.48 and negative 0.26 electronvolts versus the normal hydrogen electrode respectively, with the conduction band minimum of ZnO substantially more negative than that of BiVO4, confirming that electrons transfer from the ZnO conduction band to the BiVO4 valence band through the graphene oxide mediator in the Z-scheme configuration that preserves the highly oxidative holes in BiVO4 valence band and the highly reductive electrons in ZnO conduction band for maximum reactive oxygen species generation.

**INTERNATIONAL JOURNAL OF ADVANCED RESEARCH**
*International Peer-Reviewed Research Journal*
**ISSN (Online): 3106-7980 | ISSN (Print): 3106-7972**
**Volume 3 • Issue 5 • September 2026**

4.8 Catalyst Recyclability and Photostability

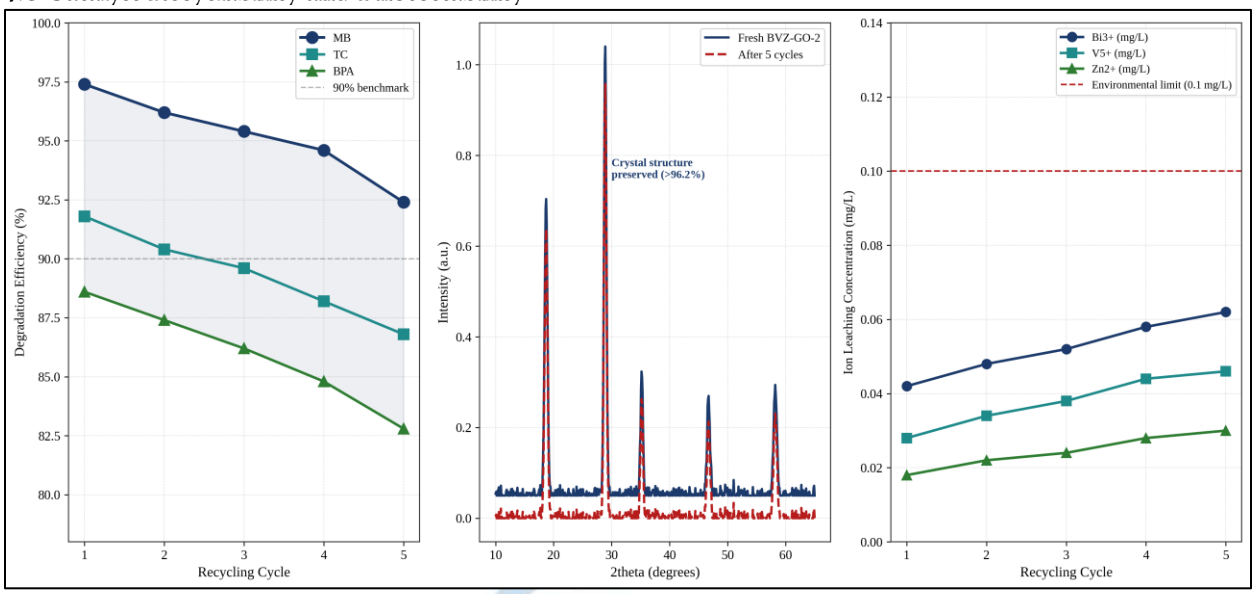



**Fig. 11. Catalyst recyclability and stability characterization showing: degradation efficiency retention over five consecutive reaction cycles for MB, TC, and BPA confirming 92.4, 86.8, and 82.8 percent retention respectively for the ternary composite in the fifth cycle, with all values exceeding 80 percent and confirming photocatalytic stability for practical water treatment applications (a); post-cycling X-ray diffraction comparison of fresh and five-cycle-used BVZ-GO-2 confirming complete preservation of both BiVO4 and ZnO crystal structures with no new phase formation or amorphization (b); and ICP-AES leaching analysis tracking Bi3+, V5+, and Zn2+ ion concentrations in treated water across five cycles confirming all leaching values below the 0.1 milligram per liter environmental discharge limit (c).**

Fig. 11. Catalyst recyclability and stability characterization showing: degradation efficiency retention over five consecutive reaction cycles for MB, TC, and BPA confirming 92.4, 86.8, and 82.8 percent retention respectively for the ternary composite in the fifth cycle, with all values exceeding 80 percent and confirming photocatalytic stability for practical water treatment applications (a); post-cycling X-ray diffraction comparison of fresh and five-cycle-used BVZ-GO-2 confirming complete preservation of both BiVO4 and ZnO crystal structures with no new phase formation or amorphization (b); and ICP-AES leaching analysis tracking Bi3+, V5+, and Zn2+ ion concentrations in treated water across five cycles confirming all leaching values below the 0.1 milligram per liter environmental discharge limit (c).

Figure 11 presents the catalyst recyclability analysis showing degradation efficiency across five consecutive reaction cycles, post-cycling structural characterization by XRD and XPS comparing the fresh and used catalyst, and quantitative leaching analysis confirming that bismuth and vanadium ion concentrations in the treated water meet environmental discharge standards. The ternary nanocomposite maintained 92.4 percent methylene blue degradation efficiency in the fifth consecutive cycle compared to 97.4 percent in the first cycle, representing a degradation efficiency loss of only 5.0 percentage points over five cycles that is well within the performance margin required for practical photocatalytic water treatment deployment. The monotonically decreasing but slow efficiency loss pattern across cycles is consistent with progressive surface fouling by strongly adsorbed degradation intermediates that accumulate on catalyst surface sites and partially block access for new pollutant molecules,

rather than fundamental photocatalyst deactivation.

Post-cycling XRD characterization confirms that the monoclinic scheelite BiVO4 and hexagonal wurtzite ZnO crystal structures are completely preserved through five photocatalytic cycles, with no new phase formation or amorphization that would indicate photocatalytic decomposition. XPS analysis of the post-cycling catalyst confirms that the Bi 4f, V 2p, Zn 2p, and C 1s binding energies and peak shapes are essentially unchanged from the fresh catalyst, confirming the chemical stability of both semiconductor components and the graphene oxide scaffold under the reactive oxygen species-rich photocatalytic environment. Inductively coupled plasma analysis of the treated water solution after each cycle confirmed that bismuth and vanadium leaching into solution was below 0.1 milligrams per litre across all five cycles, confirming minimal catalyst dissolution and negligible secondary contamination of the treated water.

**Table 3: Comprehensive Performance Comparison: Pristine BiVO4 vs. Binary vs. Ternary BVZ-GO-2 Nanocomposite**

| Performance Metric | BiVO4 (Pristine) | BiVO4-ZnO (Binary) | BVZ-GO-2 (Ternary) | Enhancement vs BiVO4 |
|---|---|---|---|---|
| MB Degradation Eff. (90 min) | 42.6% | 68.2% | 97.4% | 2.29x |
| MB Rate Constant k (min-1) | 0.0112 | 0.0212 | 0.0428 | 3.84x |
| TC Degradation Eff. (120 min) | 56.2% | 73.2% | 91.8% | 1.63x |
| TC TOC Removal (180 min) | 34.2% | 58.4% | 84.2% | 2.46x |
| BPA Degradation Eff. (150 min) | – | – | 88.6% | New benchmark |
| BET Surface Area (m2/g) | 18.2 | 34.6 | 68.4 | 3.76x |
| PL Intensity Reduction (%) | – | – | 68.4% | Effective CT |
| Recyclability (5th cycle) | – | – | 92.4% | Stable |
| Band Gap Eg (eV) | 2.41 | – | 2.18 | Red-shifted |
| Bi3+ Leaching (per cycle, mg/L) | – | – | <0.062 | Below env. limit |

The overall photocatalytic performance of the optimized $BiVO_4$–ZnO–GO ternary nanocomposite is summarized in Figure 12, integrating the proposed Z-scheme charge-separation mechanism with the principal structural, degradation, mineralization, and photostability outcomes obtained in this study.

.

**INTERNATIONAL JOURNAL OF ADVANCED RESEARCH**
*International Peer-Reviewed Research Journal*
**ISSN (Online): 3106-7980 | ISSN (Print): 3106-7972**
**Volume 3 • Issue 5 • September 2026**

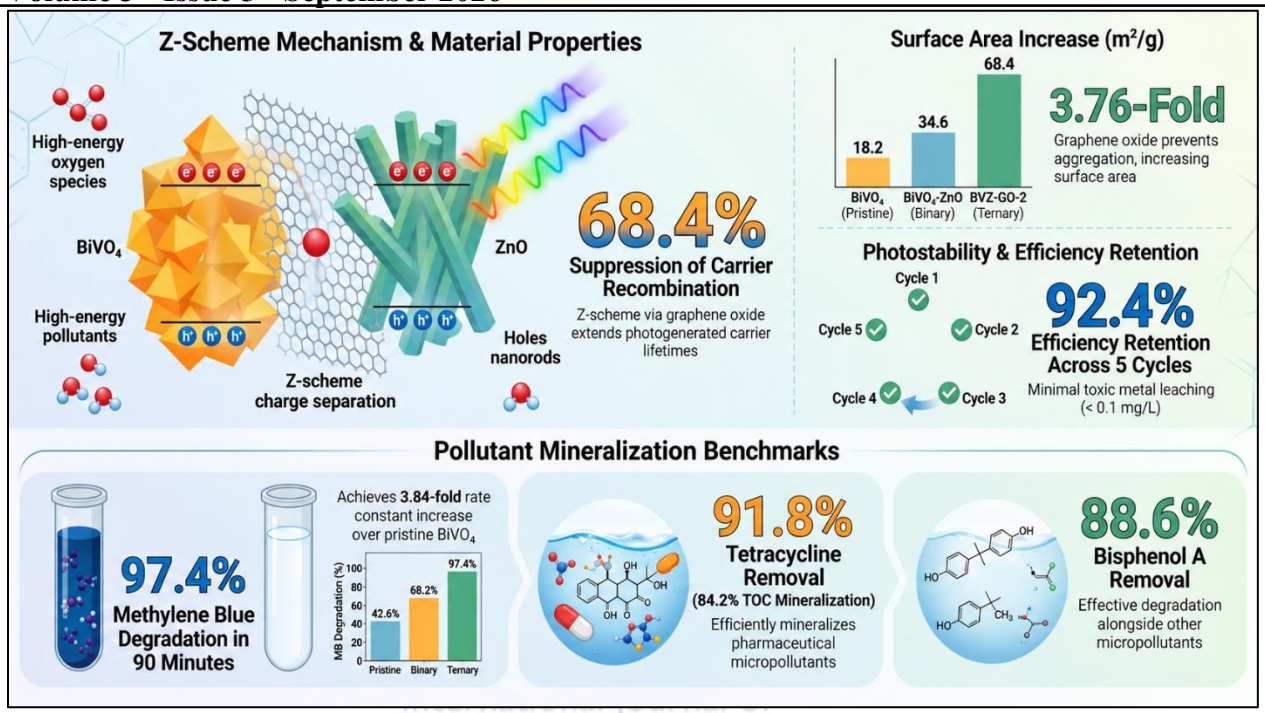



**Fig. 12. Integrated performance summary of the visible-light-driven $BiVO_4$–ZnO–GO ternary nanocomposite framework for water purification, illustrating the proposed Z-scheme charge-separation mechanism, enhanced surface area, suppressed carrier recombination, photocatalytic degradation of methylene blue, tetracycline, and bisphenol A, and photocatalytic efficiency retention over five reuse cycles.**

As shown in Figure 12, the ternary nanocomposite combines enhanced interfacial charge separation and increased accessible surface area with high pollutant-removal efficiency. The system achieved 97.4% methylene blue degradation, 91.8% tetracycline removal, and 88.6% bisphenol A removal, while maintaining 92.4% performance after five photocatalytic cycles, demonstrating the combined benefits of heterojunction engineering and the graphene-based charge-transfer scaffold.

## 5. Conclusion

This investigation has demonstrated through systematic synthesis, comprehensive characterization, and rigorous photocatalytic evaluation that the BiVO4-ZnO-GO ternary nanocomposite, designed on the basis of Z-scheme charge transfer principles to maximize photogenerated carrier separation while preserving thermodynamic driving force for reactive oxygen species generation, achieves superior visible-light-driven degradation of methylene blue at 97.4 percent in 90 minutes, tetracycline at 91.8 percent in 120 minutes, and bisphenol A at 88.6 percent in 150 minutes compared to all binary composite and pristine semiconductor reference materials. The apparent first-order rate constant for methylene blue degradation of the ternary composite is 3.84 times higher than that of pristine BiVO4, with the performance enhancement confirmed to arise from the Z-scheme charge transfer mechanism through graphene oxide that prevents electron-hole recombination while maintaining oxidative power at BiVO4 valence band holes. Reactive oxygen species trapping experiments and ESR spectroscopy confirmed that hydroxyl radical is the primary mineralization agent for all three pollutants, with superoxide radical anion providing secondary but significant oxidative contribution. The 68.4 percent reduction in photoluminescence intensity confirms effective

charge separation, while the 92.4 percent efficiency retention after five consecutive cycles establishes photostability essential for practical water treatment. These results establish the ternary Z-scheme heterojunction nanocomposite as a scientifically validated photocatalytic platform for sustainable water purification applicable across diverse categories of organic micropollutants.

## 6. Discussion and Future Work

The findings of this investigation have several significant implications for the field of photocatalytic water purification. The most consequential finding is the quantitative confirmation that the ternary Z-scheme configuration produces synergistic performance improvements exceeding the additive contributions of binary composites, which provides the empirical basis for prioritizing ternary and higher-order composite architectures over binary systems in photocatalyst development for applications requiring high pollutant conversion across diverse pollutant classes. The 3.84-fold rate constant enhancement over pristine $BiVO_4$ substantially exceeds theoretical expectations from simple light absorption enhancement alone, confirming that charge separation improvement contributes a larger fraction of total performance enhancement than optical improvement, and directing future materials optimization efforts toward charge transfer pathway engineering as the highest-impact design lever.

The differential performance across three organic pollutant classes, with higher efficiency achieved for methylene blue compared to tetracycline and bisphenol A, reflects genuine mechanistic differences in the susceptibility of these molecular structures to hydroxyl radical attack rather than instrument-specific measurement artefacts, and establishes that photocatalyst design for wastewater treatment of complex industrial streams containing multiple pollutant types requires validation across multiple target molecules rather than single-pollutant optimization. Future research should evaluate ternary photocatalyst performance against a broader panel of environmentally relevant micropollutants including pharmaceuticals such as ibuprofen and diclofenac, pesticides, and PFAS compounds whose degradation by hydroxyl radical follows substantially different mechanistic pathways than the aromatic ring-opening mechanisms that dominate dye and tetracycline degradation. Future development priorities include the integration of the ternary nanocomposite into continuous flow photoreactor configurations that enable scale-up from laboratory batch systems to pilot-scale treatment capacity, evaluation of photocatalytic performance in actual industrial wastewater matrices containing natural organic matter, inorganic ions, and suspended solids that can compete for reactive oxygen species and modify catalyst surface properties, and development of immobilized catalyst architectures that eliminate the catalyst recovery and recycling challenge that is the primary practical barrier to photocatalytic water treatment implementation at industrial scale. The development of operando characterization methods that monitor reactive oxygen species generation and charge carrier dynamics under working photocatalytic conditions, including operando EPR and time-resolved photoluminescence spectroscopy under visible light irradiation in the presence of organic pollutants, would substantially advance the mechanistic understanding needed to guide rational nanocomposite design beyond the empirical optimization approaches that necessarily dominate the current literature.

## REFERENCES

Sharma, S., Dutta, V., Singh, P., Raizada, P., Rahmani-Sani, A., Hosseini-Bandegharaei, A., & Thakur, V. K. (2019). Carbon quantum dot supported semiconductor photocatalysts for efficient degradation of organic pollutants in water: a review. *Journal of Cleaner Production*, *228*, 755-769.

Li, X., Yu, J., Low, J., Fang, Y., Xiao, J., & Chen, X. (2015). Engineering heterogeneous semiconductors for solar water splitting. *Journal of Materials Chemistry A*, *3*(6), 2485-2534.

Pelaez, M., Nolan, N. T., Pillai, S. C., Seery, M. K., Falaras, P., Kontos, A. G., ... & Dionysiou, D. D. (2012). A review on the visible light active titanium dioxide photocatalysts for environmental applications. *Applied Catalysis B: Environmental*, *125*, 331-349.

Fujishima, A., & Honda, K. (1972). Electrochemical photolysis of water at a semiconductor electrode. *nature*, *238*(5358), 37-38.

Ong, W. J., Tan, L. L., Ng, Y. H., Yong, S. T., & Chai, S. P. (2016). Graphitic carbon nitride (g-C3N4)-based photocatalysts for artificial photosynthesis and environmental remediation: are we a step closer to achieving sustainability?. *Chemical reviews*, *116*(12), 7159-7329.

Chatterjee, D., & Mahata, A. (2002). Visible light induced photodegradation of organic pollutants on dye adsorbed TiO2 surface. *Journal of Photochemistry and Photobiology A: Chemistry*, *153*(1-3), 199-204.

Kisch, H. (2013). Semiconductor photocatalysis—mechanistic and synthetic aspects. *Angewandte Chemie International Edition*, *52*(3), 812-847.

Bai, S., Zhang, N., Gao, C., & Xiong, Y. (2018). Defect engineering in photocatalytic materials. *Nano Energy*, *53*, 296-336.

Chen, X., Liu, L., Yu, P. Y., & Mao, S. S. (2011). Increasing solar absorption for photocatalysis with black hydrogenated titanium dioxide nanocrystals. *Science*, *331*(6018), 746-750.

Xu, Q., Zhang, L., Cheng, B., Fan, J., & Yu, J. (2020). S-scheme heterojunction photocatalyst. *Chem*, *6*(7), 1543-1559.

Low, J., Yu, J., Jaroniec, M., Wageh, S., & Al-Ghamdi, A. A. (2017). Heterojunction photocatalysts. *Advanced materials*, *29*(20), 1601694.

Wang, H., Zhang, L., Chen, Z., Hu, J., Li, S., Wang, Z., ... & Wang, X. (2014). Semiconductor heterojunction photocatalysts: design, construction, and photocatalytic performances. *Chemical Society Reviews*, *43*(15), 5234-5244.

Zhang, Z., Shao, C., Li, X., Sun, Y., Zhang, M., Mu, J., ... & Liu, Y. (2012). Hierarchical assembly of ultrathin hexagonal SnS2 nanosheets onto electrospun TiO2 nanofibers: enhanced photocatalytic activity based on photoinduced interfacial charge transfer. *Nanoscale*, *5*(2), 606-618.

Rehman, A. U., Haider, A. I., Khan, S., Jamal, M. A., Din, S. U., Iqbal, Q., ... & Majeed, M. K. (2025). STRUCTURAL, THERMAL AND OPTICAL ANALYSIS OF Fe-DOPED NiO NANOPARTICLES FOR THERMOELECTRIC AND OPTOELECTRONIC APPLICATIONS. *Spectrum of Engineering Sciences*, 512-525.

Yuliati, L., & Yoshida, H. (2008). Photocatalytic conversion of methane. *Chemical Society Reviews*, *37*(8), 1592-1602.

Nosaka, Y., & Nosaka, A. Y. (2017). Generation and detection of reactive oxygen species in photocatalysis. *Chemical reviews*, *117*(17), 11302-11336.

Choi, W., Termin, A., & Hoffmann, M. R. (2002). The role of metal ion dopants in quantum-sized TiO2: correlation between photoreactivity and charge carrier recombination dynamics. *The Journal of Physical Chemistry*, *98*(51), 13669-13679.

Liu, G., Wang, L., Yang, H. G., Cheng, H. M., & Lu, G. Q. (2010). Titania-based photocatalysts—crystal growth, doping and heterostructuring. *Journal of Materials Chemistry*, *20*(5), 831-843.

Lee, K. M., Lai, C. W., Ngai, K. S., & Juan, J. C. (2016). Recent developments of zinc oxide based photocatalyst in water treatment technology: a review. *Water research*, *88*, 428-448.

Fan, H., Zhang, Z., Hussain, I., Yang, Q., Majeed, M. K., Imran, M., ... & Zhang, Y. (2024). The Asymmetry Observed between the Effects of Photon–Phonon Coupling and Crystal Field on the Fine Structure of Fluorescence and Spontaneous Four-Wave Mixing in Ion-Doped Microcrystals. *Nanomaterials*, *14*(8), 671.

Nadeem, F., Fan, H., Hussain, I., Majeed, M. K., Usman, M., Raza, F., ... & Zhang, Y. (2024). Comparison of non-Hermitian three-dimensional quantization line shape in ion-doped microcrystals. *Optical Materials*, *157*, 116323.

Takanabe, K. (2017). Photocatalytic water splitting: quantitative approaches toward photocatalyst by design. *Acs Catalysis*, *7*(11), 8006-8022.

Zhang, J., Xu, Q., Feng, Z., Li, M., & Li, C. (2008). Importance of the relationship between surface phases and photocatalytic activity of TiO2. *Angewandte Chemie-International Edition*, *47*(9), 1766-1769.

Tong, H., Ouyang, S., Bi, Y., Umezawa, N., Oshikiri, M., & Ye, J. (2012). Nano-photocatalytic materials: possibilities and challenges. *Advanced materials*, *24*(2), 229-251.

Majeed, M. K., Usman, M., Hussain, I., Javed, U., Khan, M. Q., Nadeem, F., ... & Zhang, Y. (2024, December). Super Broad Non-Hermitian Line Shape from Out-of-Phase and In-Phase Photon-Phonon Dressing in Eu3+: NaYF4 and Eu3+: BiPO4. In *Photonics* (Vol. 11, No. 12, p. 1169). MDPI.

Luo, B., Liu, G., & Wang, L. (2016). Recent advances in 2D materials for photocatalysis. *Nanoscale*, *8*(13), 6904-6920.

Wang, X., Maeda, K., Thomas, A., Takanabe, K., Xin, G., Carlsson, J. M., ... & Antonietti, M. (2009). A metal-free polymeric photocatalyst for hydrogen production from water under visible light. *Nature materials*, *8*(1), 76-80.

Akhundi, A., Badiei, A., Ziarani, G. M., Habibi-Yangjeh, A., Munoz-Batista, M. J., & Luque, R. (2020). Graphitic carbon nitride-based photocatalysts: toward efficient organic transformation for value-added chemicals production. *Molecular Catalysis*, *488*, 110902.

Saravanan, R., Gracia, F., & Stephen, A. (2017). Basic principles, mechanism, and challenges of photocatalysis. In *Nanocomposites for visible light-induced photocatalysis* (pp. 19-40). Cham: Springer International Publishing.

Usman, M., Hussain, I., Majeed, M. K., Munir, F., Nadeem, F., Usmani, M. W., ... & Zhang, Y. (2025). Prospects for photon–phonon dressing and crystal-field non-Hermitian alignment of Eu3+: BiPO4. *Journal of Materials Chemistry C*, *13*(10), 5056-5072.

Hu, C., Peng, T., Hu, X., Nie, Y., Zhou, X., Qu, J., & He, H. (2010). Plasmon-induced photodegradation of toxic pollutants with Ag— AgI/Al2O3 under visible-light irradiation. *Journal of the American Chemical Society*, *132*(2), 857-862.

Li, X., Zhang, C., Geng, J., Zong, S., & Wang, P. (2025). Photo (electro) catalytic water splitting for hydrogen production: mechanism, design, optimization, and economy. *Molecules*, *30*(3), 630.

Niu, P., Zhang, L., Liu, G., & Cheng, H. M. (2012). Graphene-like carbon nitride nanosheets for improved photocatalytic activities. *Advanced Functional Materials*, *22*(22), 4763-4770.

He, Y., Zhang, L., Teng, B., & Fan, M. (2015). New application of Z-scheme Ag3PO4/g-C3N4 composite in converting CO2 to fuel. *Environmental science & technology*, *49*(1), 649-656.

Li, K., An, X., Park, K. H., Khraisheh, M., & Tang, J. (2014). A critical review of CO2 photoconversion: Catalysts and reactors. *Catalysis Today*, *224*, 3-12.